

# Wake development in staggered short cylinder arrays within a channel

Jason K. Ostanek · Karen A. Thole

Received: 30 August 2011 / Revised: 8 April 2012 / Accepted: 28 April 2012  
© Springer-Verlag 2012

**Abstract** Staggered arrays of short cylinders, known as pin–fins, are commonly used as a heat exchange method in many applications such as cooling electronic equipment and cooling the trailing edge of gas turbine airfoils. This study investigates the near wake flow as it develops through arrays of staggered pin fins. The height-to-diameter ratio was unity while the transverse spacing was kept constant at two cylinder diameters. The streamwise spacing was varied between 3.46 and 1.73 cylinder diameters. For each geometric arrangement, experiments were conducted at Reynolds numbers of  $3.0 \times 10^3$  and  $2.0 \times 10^4$  based on cylinder diameter and velocity through the minimum flow area of the array. Time-resolved flowfield measurements provided insight into the dependence of row position, Reynolds number, and streamwise spacing. Decreasing streamwise spacing resulted in increased Strouhal number as the near wake length scales were confined. In the first row of the bundle, low Reynolds number flows were mainly shear-layer-driven while high Reynolds number flows were dominated by periodic vortex shedding. The level of velocity fluctuations increased for cases having stronger vortex shedding. The effect of streamwise spacing was most apparent in the reduction of velocity fluctuations in the wake when the spacing between rows was reduced from 2.60 diameters to 2.16 diameters.

## List of symbols

$d_p$	Tracer particle diameter
$D$	Pin–fin diameter
$D_h$	Duct hydraulic diameter
$E_{uu}$	One-dimensional energy spectrum of streamwise velocity
$f$	Frequency
$H$	Channel height, pin–fin height
$k$	Turbulent kinetic energy
$L_r$	Wake closure position
$Re_D$	Reynolds number, $Re_D = U_{\max} D \nu^{-1}$
$S_L$	Longitudinal/streamwise pin–fin spacing (X-direction)
$S_T$	Transverse pin–fin spacing (Y-direction)
$St$	Strouhal number, $St = f D U_{\max}^{-1}$
$Stk$	Stokes number, $Stk = (d_p \rho_p / 18 \mu) (U_{\max} / D)$
$U_m$	Time-mean bulk channel velocity
$U_{\max}$	Time-mean velocity through minimum array flow area
$\bar{U}$	Local time-averaged streamwise velocity
$u'$	Local fluctuating streamwise velocity, or RMS velocity
$\bar{V}$	Local time-averaged transverse velocity
$v'$	Local fluctuating transverse velocity, or RMS velocity
$X$	Longitudinal/streamwise direction
$Y$	Transverse direction
$Z$	Wall-normal direction

## Greek symbols

$\rho_p$	Tracer particle density
$\nu$	Air kinematic viscosity
$\mu$	Air dynamic viscosity
$\tilde{\omega}_Z$	Instantaneous Z-vorticity
$\phi$	Phase angle

J. K. Ostanek (✉) · K. A. Thole  
Mechanical and Nuclear Engineering Department,  
The Pennsylvania State University,  
University Park, PA, USA  
e-mail: jason.ostanek@navy.mil

K. A. Thole  
e-mail: kthole@enr.psu.edu

## 1 Introduction

Arrays of circular cylinders are a common configuration used in heat exchangers. Long height-to-diameter cylindrical arrays, which are commonly used in nuclear power plants (fuel rod bundles) and boilers, are typically bounded by two endwalls that are spaced sufficiently far apart such that end effects are negligible. In heat sinks used for compact electronics, pin–fin arrays typically include one end that is constrained by a solid wall while the other end is unconstrained. Heat exchangers used in cooling gas turbine airfoils feature pin–fin arrays constrained by two solid boundaries (endwalls) in close proximity to one another. The present work considers the case having short cylinders (pin–fins) confined to a channel having two boundaries in close proximity. Pin–fin height-to-diameter ratios near unity are common because of geometrical constraints imposed by the characteristically narrow trailing edge of turbine blades. The flow in pin–fin arrays is a challenging topic since there are interactions between endwall boundary layers, pin–fin boundary layers, and separated flow in the wake. While pin–fin heat transfer has been studied over the past several decades, little work has been done to understand the fluid mechanics driving the heat transfer in pin–fin arrays.

For many industrial applications, long cylinder banks are designed using semi-empirical models. Unfortunately, the well-established models developed for long cylinders do not apply to pin–fins because of the influence of the bounding channel walls (Metzger et al. 1982). Computational fluid dynamics is another design tool commonly used to predict the performance of pin–fin arrays; however, the most economical turbulence models (Reynolds-averaged Navier–Stokes turbulence models) do not reliably predict the separated flows in pin–fin arrays. Because pin–fin channels rely on turbulent mixing to augment heat transfer, better heat exchanger performance may be achieved through experimental investigation of the turbulent flowfield. By understanding the fluid mechanics, pin–fin heat exchangers may be designed to take advantage of the turbulent flow present in pin–fin arrays.

Pin–fins augment heat transfer in a channel by disturbing the endwall boundary layers and by increasing convective surface area. The endwall boundary layer is disturbed by the formation of a horseshoe vortex at the junction between pin–fin and endwall. Many researchers have deduced the formation of a horseshoe vortex in measurements of heat transfer (Ames et al. 2007; Lyall et al. 2011; Lawson et al. 2011; Chyu et al. 2009). Ozturk et al. (2008) actually visualized the horseshoe vortex for a single pin–fin having  $H/D = 0.6$ . The horseshoe vortex was highly unsteady and was asymmetric at any given instant in time. Pin–fins also disturb the duct flow by

generating turbulence in the near wake, mainly as a result of vortex shedding. The fluctuating lift coefficient, an indication of vortex shedding strength, was found to increase for a single pin–fin in a channel when  $H/D$  was increased from 0.25 to 1.0 (Szepessy and Bearman 1992). Fluctuating lift coefficient peaked at  $H/D = 1.0$ , then decreased as  $H/D$  was increased above  $H/D = 1.0$ . In a multiple-row pin–fin array, increasing aspect ratio was found to benefit heat transfer (Chyu et al. 2009). Increasing aspect ratio provided an increase in convective area. It was unclear, however, whether increasing the aspect ratio also enhanced heat transfer by altering the vortex shedding mechanics as Szepessy and Bearman (1992) observed.

Pin–fin flows depend on streamwise spacing,  $S_L/D$ , and transverse spacing,  $S_T/D$ , in addition to cylinder aspect ratio. For long cylinder arrays, shedding frequency increased with decreased cylinder spacing since the near wake length was constrained (Weaver et al. 1993; Polak and Weaver 1995; Oengoren and Ziada 1998). Additionally, the mean static pressure on the cylinder showed a significantly different distribution, indicating a change in flowfield behavior, for closely spaced arrays (Aiba et al. 1982; Zdravkovich and Namork 1979). For pin–fin arrays, few studies directly measure the flowfield, but heat transfer measurements give an indication of the behavior of the flow. Lyall et al. (2011) found that increased transverse spacing,  $S_T/D$ , for a single row of pin–fins reduced heat transfer as a consequence of having less coverage from the enhancement of the horseshoe vortex and wake turbulence. For  $S_T/D = 2$ ,  $H/D = 1$ , and  $Re_D = 5.0e3$ , heat transfer contours in the wakes of adjacent pin–fins were observed to merge within a few diameters. At higher Reynolds numbers and wider spacings, however, heat transfer contours in the wakes of adjacent pin–fins remained separated. For multiple-row pin–fin arrays, Lawson et al. (2011) found results consistent with Lyall et al. (2011) because increased spacing,  $S_T/D$  and  $S_L/D$ , resulted in decreased heat transfer. Row-averaged heat transfer increased through the fourth row for  $S_T/D = 2$ ,  $S_L/D = 1.73$ ,  $H/D = 1$ , in agreement with a similar configuration reported by Metzger et al. (1982). As  $S_L/D$  was increased to 3.46, however, row-averaged heat transfer only increased through the second row. Lyall et al. (2011) and Lawson et al. (2011) showed that varying pin–fin spacing may significantly alter heat transfer in the near wake. It was unclear, however, whether heat transfer performance was driven mainly by convective area or by changes in the turbulent wake.

Flowfield measurements have been performed for a pin–fin array having  $S_T/D = 2.5$ ,  $S_L/D = 2.5$ , and  $H/D = 2$  (Ames and Dvorak 2006a, b; Ames et al. 2007; Delibra et al. 2010). Detailed measurements have provided valuable information throughout the pin–fin array such as shedding frequency, turbulent energy spectrum, and turbulent

dissipation rate. Ames and Dvorak (2006b) found that vortex shedding was present in the first row wakes and unsteadiness increased with increasing Reynolds number. Turbulence was found to peak around the fourth row then decrease to a constant value in downstream rows consistent with previous researchers (Metzger and Haley 1982; Simoneau and VanFossen 1984). Delibra et al. (2010) mentioned that large-scale motions generated in the wake as well as enhanced turbulent mixing from small-scale motions play a role in heat transfer, although the specific mechanism for heat transfer was not explicitly stated. While detailed experiments and computations have provided valuable insights into a common pin–fin configuration, the spatio-temporal development of the near wake and the influence of the near wake behavior on heat transfer remained unclear.

A survey of relevant literature has shown that the flow in pin–fin arrays is complicated by the presence of endwall boundary layers, pin–fin boundary layers, and separated wake flow. The present study will clarify how pin–fin flow features interact throughout the array and how these interactions affect the near wake dynamics. Using time-resolved measurement techniques, the present study will investigate the near wake development through pin–fin arrays of various streamwise spacing,  $S_L/D$ , and Reynolds number,  $Re_D$ . The results from the present study may be used to aid the design of pin–fin heat exchangers and to validate numerical models.

## 2 Experimental facility and instrumentation

### 2.1 Test facility

Experiments were carried out at steady-state in a closed-loop, recirculating channel, shown in Fig. 1. Air was circulated through the facility using an electric fan with a variable frequency drive. The flow was conditioned using two large settling chambers, equipped with splash plates, on either side of the test section to ensure uniform flow across the width of the duct. A heat exchanger installed in one of the settling chambers allowed for the inlet temperature to be held constant. Relief valves, installed upstream

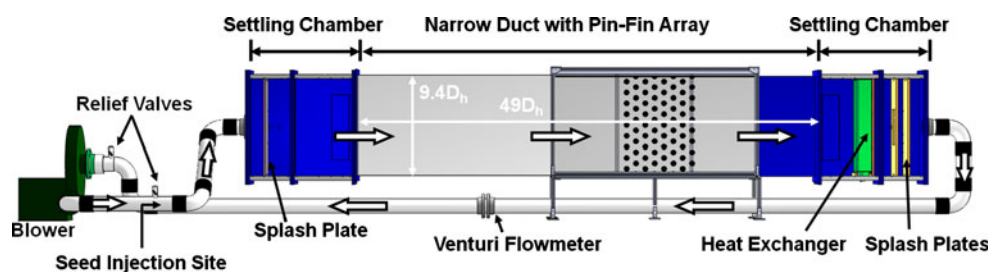
and downstream of the blower, were used to adjust the gage pressure within the measurement section. Experiments were performed such that the gage pressure in the test section was nearly zero to minimize the potential for leaks and to minimize deformation of the channel walls. The test section was a rectangular duct having height of 63.5 mm (0.53 hydraulic diameters), width of 1.13 m (9.4 hydraulic diameters), and length of 5.87 m (49 hydraulic diameters). The cylinders, which spanned the height of the channel, had a diameter of 63.5 mm to give an aspect ratio of  $H/D = 1$ . A portion of the measurement section was optically accessible to allow the use of time-resolved, digital particle image velocimetry (TRDPIV). In Fig. 2, the inlet boundary layer was measured and validated against published values for fully developed turbulent duct flow (Ostaneck and Thole 2011).

In each experiment, the transverse spacing of the staggered cylinders was  $S_T/D = 2$  measured from center-to-center. Figure 3 shows a scale drawing of the measurement section containing the pin–fins. Nine full cylinders were placed across the width of the duct to ensure periodicity in the transverse direction. In even-numbered rows, eight full cylinders plus two half-cylinders were placed across the width of the duct. In the streamwise direction, seven rows of cylinders were installed for a total of 63 cylinders. The streamwise spacing was varied between a lower limit of  $S_L/D = 1.73$  and an upper limit of  $S_L/D = 3.46$ . These limits were divided evenly to give 3 intermediate spacings of  $S_L/D = 2.16, 2.60, \text{ and } 3.03$ . It should be noted that a single row of cylinders was included in the test matrix to provide a baseline case having no downstream cylinders (giving a streamwise spacing of  $S_L/D = \infty$ ).

### 2.2 Time-resolved digital particle image velocimetry

Instantaneous realizations of the near wake flow were captured using a commercially available TRDPIV system. A dual cavity 15 W Nd:YAG laser capable of firing at 10 kHz per laser cavity illuminated the tracer particles while a 2 kHz CMOS camera captured particle images at a spatial resolution of  $1,024 \times 1,024$  pixels. Di-Ethyl-Hexyl Sebecat (DEHS) was atomized and injected upstream of the measurement section to provide tracer particles for

**Fig. 1** Schematic of closed-loop, recirculating channel used to experimentally investigate the flow through pin–fin heat exchangers



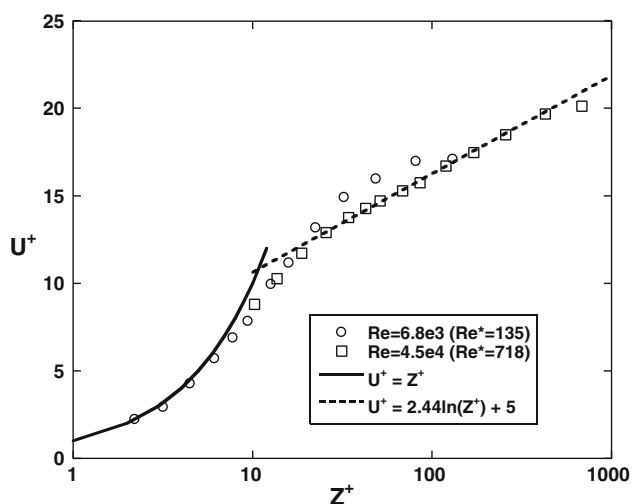


**Fig. 2** Inlet boundary layer measured upstream of the pin-fins. Good agreement with the law-of-the-wall was observed for low and high Reynolds numbers (Ostaneck and Thole 2011)

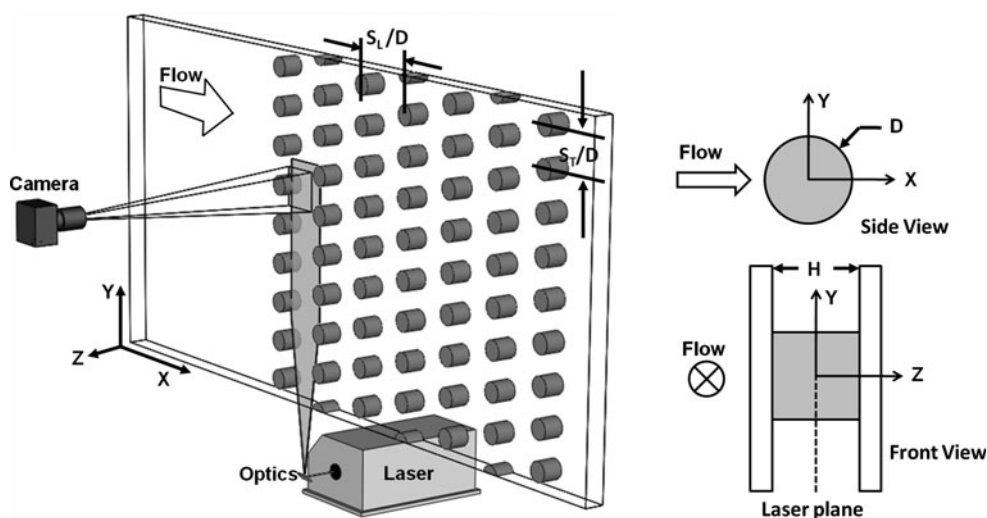
TRDPIV measurements. Because the test facility was a closed-loop system, the flow became fully seeded in a very short amount of time. The Stokes number of the DEHS particles was calculated to be  $Stk = 3e-4$ , validating the approximation that the tracer particles follow the flow. The time delay between laser pulses was adjusted for each run to obtain an optimal particle displacement across the field of view. Because of the large dynamic range of the near wake flow, particles in the core flow typically had a displacement around 16 pixels while particles inside the wake had displacement of only a few pixels. In every test case, the maximum particle displacement was less than one-fourth of the initial interrogation window size. A 105 mm lens was used with a camera standoff distance of 0.46 m to capture a viewing area of 127 by 127 mm at 7.6 pixels/mm resolution. The Kármán vortices, which had length scale of

approximately  $1D$ , were resolved by 483 pixels and 60 velocity vectors. The shear layer eddies, which had length scale of approximately  $0.1D$ , were resolved by 48.3 pixels and 6 velocity vectors.

TRDPIV measurements were made in the X–Y plane at the midspan of the duct,  $Z/H = 0$ . While three-dimensional effects are important in pin–fin channels, the main goal of the present work was to characterize the effect of stream-wise spacing on the near wake. Performing measurements at the midspan was the logical choice for accomplishing this goal because several previous pin–fin studies indicated that the time-mean flowfield is approximately two-dimensional across the majority of the center portion of the duct (Ames and Dvorak 2006a). To minimize reflections of the laser sheet, the pin–fins were painted flat black which allowed measurements to be taken very close to the pin–fin surface. The camera was aligned with the Z-axis, orthogonal to the laser plane. Figure 3 shows the TRDPIV system and its orientation within the test facility. Flow statistics were calculated over 3,000 image pairs at  $1,024 \times 1,024$  pixel resolution. For the low Reynolds number case,  $Re_D = 3.0e3$ , the sampling rate was 100 Hz. The Nyquist frequency of 50 Hz was 21 times greater than the vortex shedding frequency and the bulk flow crossed the domain 88 times. At high Reynolds number,  $Re_D = 2.0e4$ , the sampling rate was 1 kHz. The Nyquist frequency of 500 Hz was 31 times greater than the vortex shedding frequency and the bulk flow crossed the domain 59 times.

Particle images were processed using commercial software, DaVis 7.2, included with the TRDPIV system from LaVision Inc. ([www.Lavision.de](http://www.Lavision.de), 2011). The first operation performed on particle images was a minimum pixel intensity background subtraction to improve signal-to-noise ratio. A standard cross-correlation was then used to obtain particle displacement vectors among image pairs. To improve accuracy and reduce pixel locking, a

**Fig. 3** Drawing of the TRDPIV system and its orientation within the experimental facility. TRDPIV measurements were made at the midspan of the channel,  $Z/H = 0$



decreasing multi-grid scheme was used with fractional window offset and first-order window deformation. The first-order window deformation technique uses previously calculated vector fields to deform the interrogation windows to more accurately track the motion of particles in regions of large velocity gradients. The maximum measurable displacement gradient increases from  $\sim 0.2$  pixels/pixel for standard windowing to 0.5 pixels/pixel for the first-order deformation technique (Scarano and Riethmuller 2000). In effect, the first-order deformation technique extends the dynamic range of the image processing because a larger time step may be used between image pairs without suffering significant in-plane, loss-of-pairs. The maximum displacement gradient observed in the present work was 0.4 pixels/pixel which justified the use of the first-order deformation technique. Before obtaining particle displacement vectors, however, regions outside of the flow domain were masked and zero-padded. Zero-padding was performed on the initial pass if a given window was at least 30 % masked and was performed on all subsequent passes if a given window was at least 60 % masked. Vector validation was performed after each pass using a 4-pass median filter (Nogueira et al. 1997) with adjustable criteria for removal and re-insertion of possible spurious vectors. For each experiment, the vector validation scheme was checked to ensure that only spurious vectors were removed.

### 2.3 Uncertainty analysis

Uncertainty in mean flow statistics such as Reynolds number and bulk channel velocity was estimated using the sequential perturbation method (Moffat 1988). The sequential perturbation method uses a root-sum-square calculation for combining individual sources of uncertainty into an overall uncertainty for some parameter of interest, such as Reynolds number or bulk velocity. At 95 % confidence level, the maximum uncertainty in Reynolds number and bulk velocity was 2.0 and 1.9 %, respectively.

Uncertainty in PIV measurements was estimated based on several possible sources of error. First, when using a fractional window offset and first-order window deformation, the maximum measurable displacement gradient is 0.5 pixels/pixel (Scarano and Riethmuller 2000). The maximum observed displacement gradient was  $\partial U/\partial Y = 0.4$  pixels/pixel and  $\partial V/\partial X = 0.1$  pixels/pixel, such that no gradient truncation occurred. Another possible source of error was random error in the location of the correlation peak as a function of displacement gradient (Scarano and Riethmuller 2000). Using fractional window offset and first-order window deformation, a maximum random error of  $\varepsilon = 0.15$  pixels and 0.03 pixels was estimated for the  $U$  and  $V$  components, respectively (Scarano and Riethmuller 2000). The instantaneous and time-averaged

velocity components had uncertainty of 2.0 % for the  $U$  component and 0.4 % for the  $V$  component. The in-plane Reynolds stress components had uncertainty of 8 % for  $\langle u'u' \rangle$ , 2 % for  $\langle v'v' \rangle$ , and 5.2 % for  $\langle u'v' \rangle$ . Uncertainty in vorticity was quantified using the same technique where random error in the locations of correlation peaks in adjacent windows caused uncertainty in the instantaneous velocity gradient. Using fractional window offset and first-order window deformation, a maximum random error of  $\varepsilon = 0.042$  pixels/pixel and 0.006 pixels/pixel was estimated for  $\partial U/\partial Y$  and  $\partial V/\partial X$ , respectively (Scarano and Riethmuller 2000). The resulting uncertainty in instantaneous and time-averaged vorticity was 3.3 %.

## 3 Results and discussion

### 3.1 Effect of streamwise spacing on time-mean flowfield

Although heat transfer in the near wake depends on many factors, detailed measurements have shown that heat transfer in the wake of the pin-fins correlates with the size of the recirculation region (Ames et al. 2007; Ostanek and Thole 2011; Lyall et al. 2011). To characterize the length scale of the near wake in the present work, the wake closure position,  $L_r/D$ , was defined as the position of zero time-mean streamwise velocity along the wake axis (often referred to as the length of the recirculating region). Figure 4 shows the wake closure position as a function of Reynolds number for the single row of pin-fins having  $S_T/D = 2$  and  $H/D = 1$ . As indicated in Fig. 4, the wake closure length for the single row of pin-fins was reduced relative to a single, infinite cylinder (Norberg 1998) by 6 %

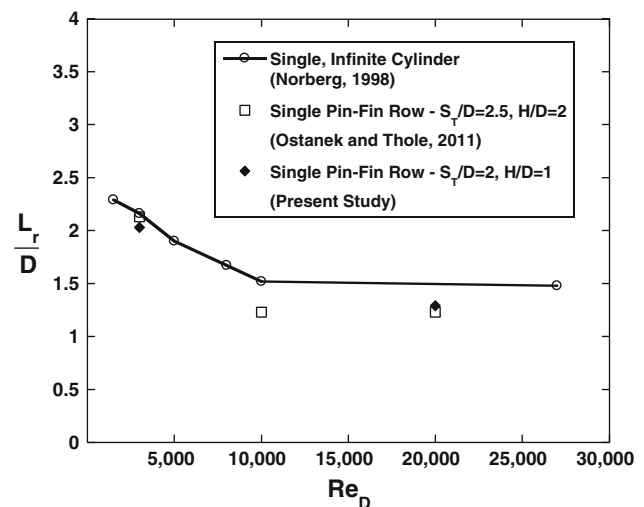


**Fig. 4** Wake closure position,  $L_r/D$ , versus  $Re_D$  for single row pin-fin wakes and single, infinitely long cylinders

and 10 % at  $Re_D = 3.0e3$  and  $2.0e4$ , respectively. The single row pin-fins having  $S_T/D = 2$ ,  $H/D = 1$  were in good agreement with a similar single row of pin-fins having  $S_T/D = 2.5$ ,  $H/D = 2$  (Ostaneck and Thole 2011). At low Reynolds number, both of the single pin-fin rows had similar wake closure position to that of a single, infinite cylinder. At high Reynolds number, however, both of the single pin-fin rows showed reduced wake closure length relative to the single, infinite cylinder. The single row pin-fins were subjected to incoming wall-generated turbulence, whereas the single, infinite cylinder presented in Fig. 4 was subjected to low freestream turbulence intensity of less than 0.1 % (Norberg 1998). It is well known that the wake closure position correlates with the spreading (mixing) along the shear layers emerging tangent to the cylinder (Zdravkovich 1997). Increasing Reynolds number and turbulence intensity both increase turbulent mixing along the shear layer, and the wake closure position, subsequently, decreases. The literature for single, infinite cylinders has shown that the wake closure position is insensitive to elevated freestream turbulence at low Reynolds numbers ( $Re_D = 3.0e3$ ) while elevated freestream turbulence has been shown to decrease the wake closure position at higher Reynolds numbers ( $Re_D = 8.0e3$ ) (Zdravkovich 1997). Because viscous effects were more important at low Reynolds numbers, the shear layer was less influenced by incoming disturbances when compared to high Reynolds numbers. In the context of the present work, wall-generated turbulence was unable to influence the shear

layer for  $Re_D = 3.0e3$  which resulted in a similar wake closure position when comparing a single pin-fin row to that of a single, infinite cylinder under low freestream turbulence as shown in Fig. 4.

To compare the wake closure length in pin-fin arrays having multiple rows, Fig. 5 shows  $L_r/D$  as a function of streamwise spacing,  $S_L/D$ , and row position. First row wakes are shown in Fig. 5a, while third row wakes are shown in Fig. 5b. For comparison, the first row wakes were compared with a single, infinite cylinder (Norberg 2003) and several examples of long-tube cylinder banks (Paul et al. 2007; Iwaki et al. 2004). The third row wakes of the present pin-fin arrays were also compared with the long-tube cylinder banks. In general, the wake closure position decreased with increasing Reynolds number, as previously described. The wake closure position also decreased when comparing the third row wakes with first row wakes. As mentioned previously, increased mixing along the shear layers corresponded with a decreased wake closure position. The disturbances generated in the first row wakes influenced the third row shear layers (and wakes). In the previous discussion, the elevated turbulence encountering a single pin-fin row was unable to overcome the viscous effects at low Reynolds number. The third row wake closure positions showed that the disturbances from the first row wake were much more significant than the disturbances generated in the unobstructed duct, and the disturbances generated in the first row affected the third row wake closure position for both low and high Reynolds

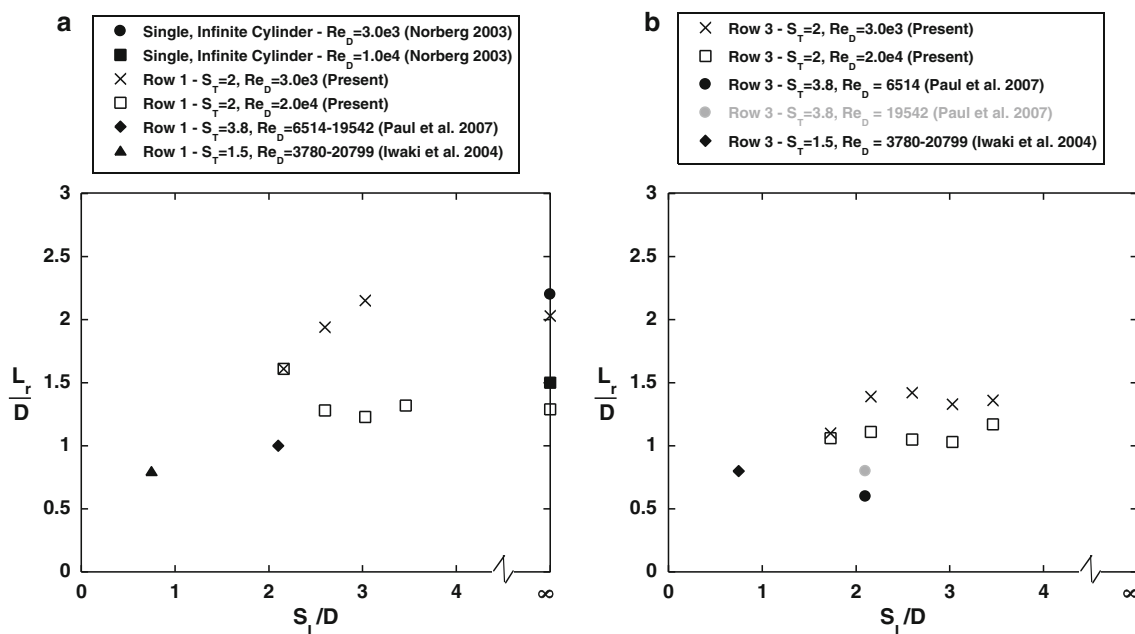


**Fig. 5** Wake closure position,  $L_r/D$ , as a function of  $S_L/D$  and  $Re_D$  for the **a** first and **b** third row wakes. The single pin-fin row and single, infinite cylinder have  $S_L/D = \infty$  since there are no downstream pin-

fins. Those wakes having  $L_r/D$  outside the TRDPIV viewing window were omitted

number. When compared to long-tube cylinder banks, the pin–fin flows showed a longer wake closure position in both first and third row wakes. The differences between pin–fins and long-tube cylinder banks require further investigation, although it was likely that three-dimensional effects in the pin–fin channel contributed to the differences.

Streamlines of the time-averaged flowfields are shown in Figs. 6 and 7 for  $Re_D = 3.0e3$  and  $2.0e4$ , respectively. The wake closure positions presented in Figs. 4 and 5 are indicated in Figs. 6 and 7 with dashed lines, allowing for comparison between different streamwise spacings and Reynolds numbers. In Fig. 6, the presence of the second row pin–fins was found to alter the first row wakes at

$Re_D = 3.0e3$  even for the widest streamwise spacing of  $S_L/D = 3.46$ . The wake was elongated for the first row of  $S_L/D = 3.46$  in comparison with the single row of pin–fins because a favorable pressure gradient was created by the jet *between* second row cylinders which provided a suction force on the first row wake of  $S_L/D = 3.46$ . As  $S_L/D$  was reduced below 3.46, the wake length was reduced, indicating that the adverse pressure gradients in *front* of second row pin–fins began to overcome the favorable pressure gradient *between* second row pin–fins. The third row wake closure positions were less dependent on streamwise spacing when compared with the first row wakes.

**Fig. 6** Mean streamlines for each geometric configuration at  $Re_D = 3.0e3$ . Dashed lines indicate position of wake closure. Dashed lines were omitted if  $L_r/D$  fell outside the TRDPIV viewing window

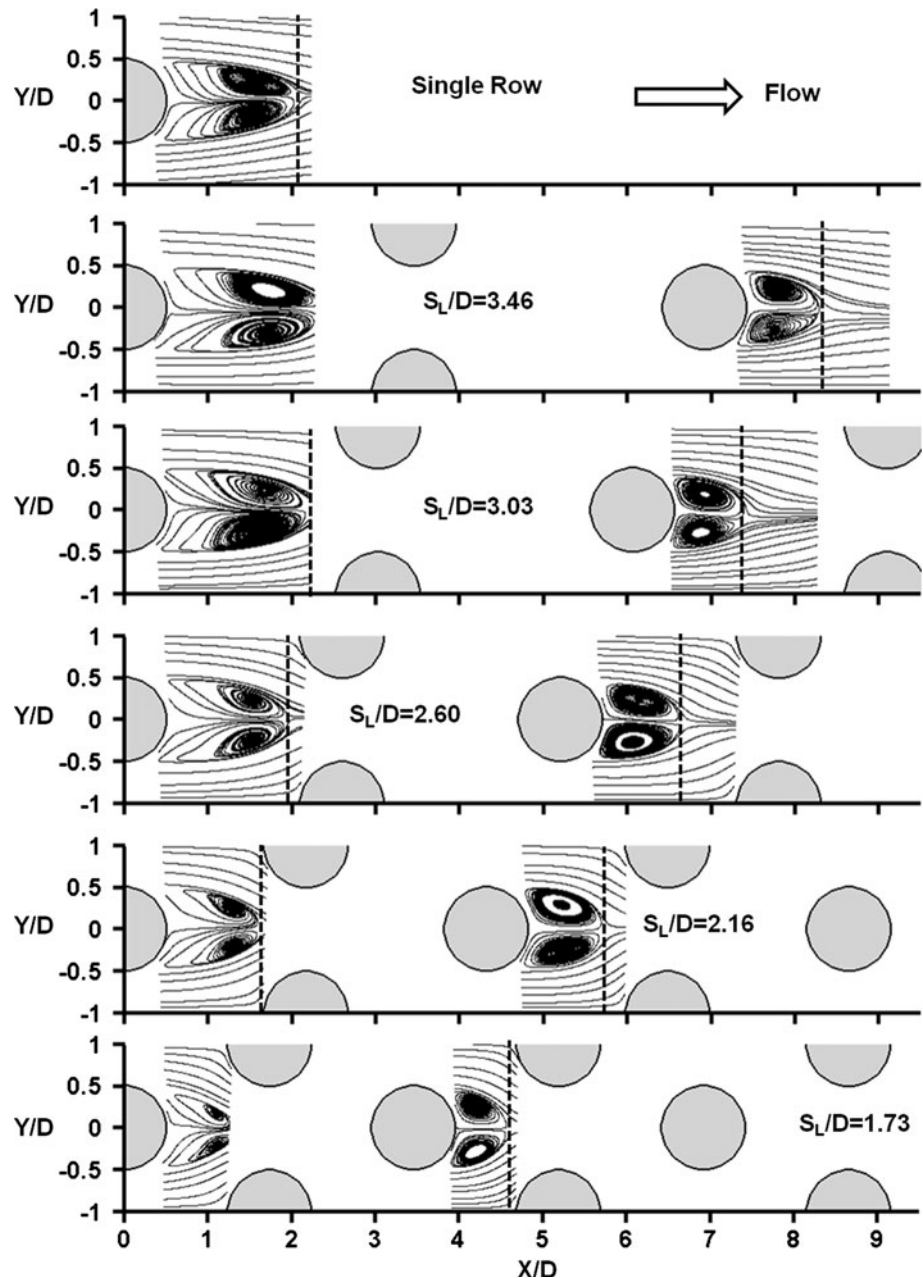
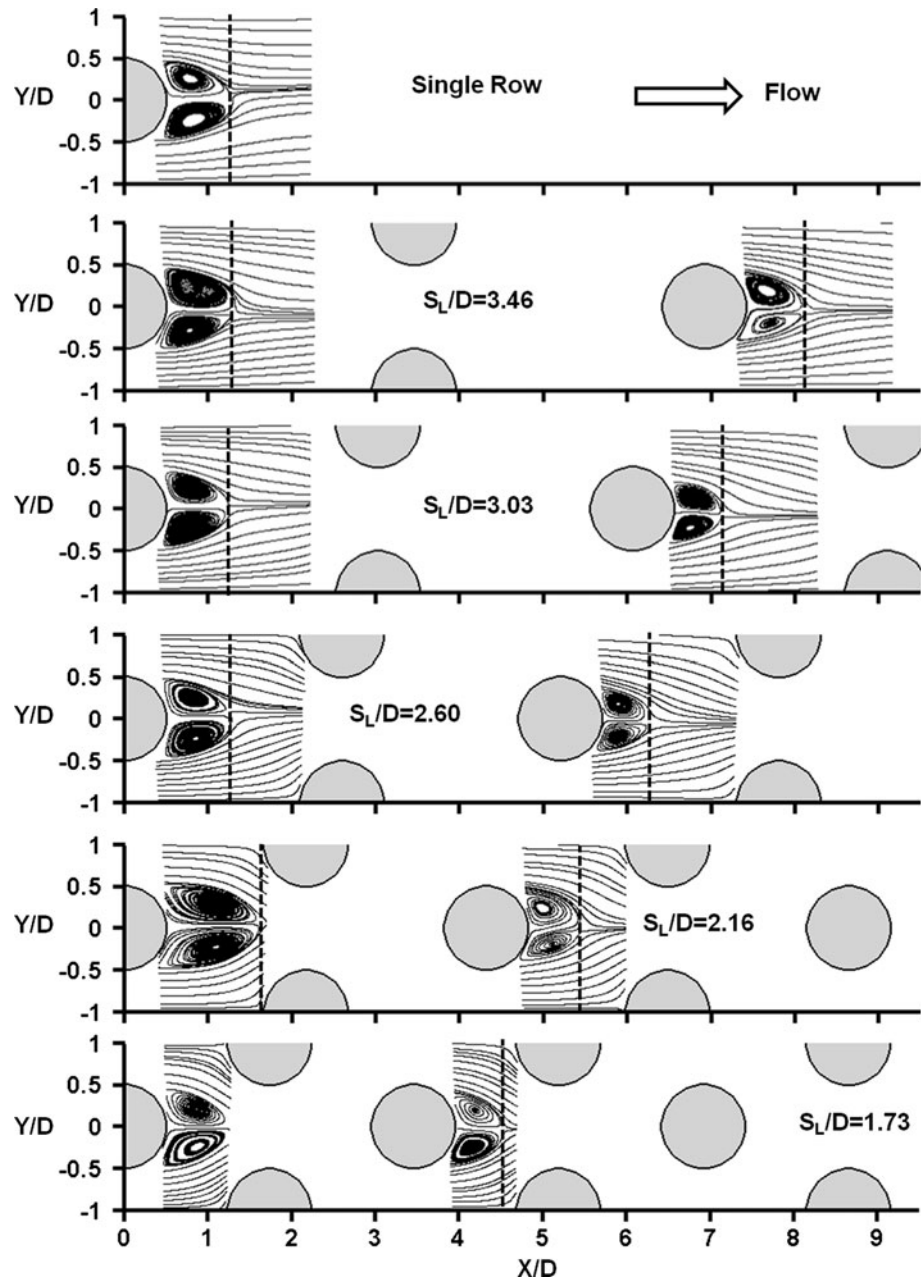


**Fig. 7** Mean streamlines for each geometric configuration at  $Re_D = 2.0e4$ . Dashed lines indicate position of wake closure. Dashed lines were omitted if  $L_r/D$  fell outside the TRDPIV viewing window



When Reynolds number was increased to  $2.0e4$ , the first row wake closure position was nearly constant with streamwise spacing as shown in Fig. 7. The first row wakes were shortened at  $Re_D = 2.0e4$  relative to  $3.0e3$  because of decreased shear layer stability, as discussed previously. The first row wakes at  $Re_D = 2.0e4$  showed no significant influence from the presence of the second row for  $S_L/D > 2.16$ . At  $S_L/D = 2.16$ , however, the first row wake was elongated from the favorable pressure gradient generated between second row pin-fins. For  $S_L/D = 1.73$ , the adverse pressure gradient from second row pin-fins caused the first row wake to be shortened relative to that of

$S_L/D = 2.16$ . As with  $Re_D = 3.0e3$ , the third row wakes at  $Re_D = 2.0e4$  were shortened relative to the first row wakes because of disturbances generated in upstream rows.

The time-averaged velocity profiles were compared at selected locations in the wake to gain more insight into the near wake behavior. Figures 8 and 9 show time-averaged velocity components measured at  $X/D = 1$ ,  $Z/H = 0$  (channel symmetry plane), and  $-1 \leq Y/D \leq 1$  for  $Re_D = 3.0e3$  and  $2.0e4$ , respectively. At  $Re_D = 3.0e3$ , time-averaged streamwise velocity across the first row wakes (Fig. 8a) showed a large velocity gradient along the shear layer while the third row wakes (Fig. 8b) showed a much smoother

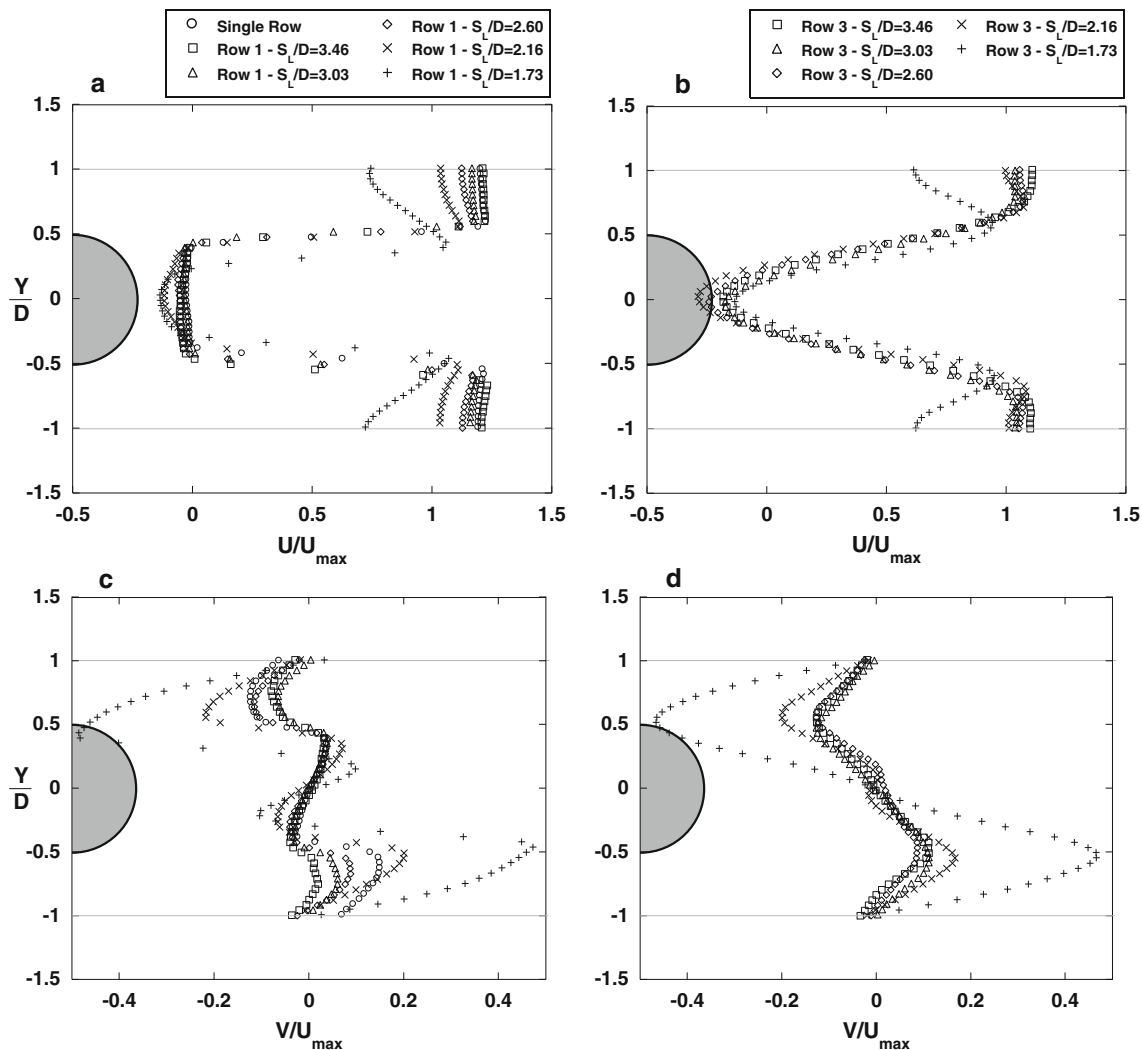


**Fig. 8** Mean velocity extracted at  $X/D = 1.0$  and  $Z/H = 0$  (channel symmetry plane) for  $Re_D = 3.0e3$ . Mean streamwise velocity for first and third row wakes is shown in (a) and (b), respectively. Mean

transverse velocity for first and third row wakes is shown in (c) and (d), respectively. Legends are common between (a) and (c) and between (b) and (d)

velocity profile across the wake. The presence of increased turbulence in the third row caused increased mixing and a reduction in the strength of the time-mean velocity gradients in comparison with the first row. The time-averaged transverse velocity profiles clearly illustrated the effect of streamwise spacing on the turning of the flow in upstream wakes. For  $S_L/D = 1.73$ , for example, there was a strong turning of the flow, shown profiles of  $\bar{V}$  in Fig. 8c and d. At  $Re_D = 2.0e4$ , in Fig. 9, the streamwise velocity gradients in both first and third row wakes were smoothed relative to that of the first row wakes at  $Re_D = 3.0e3$ . Increased turbulent mixing was present at high Reynolds numbers, even in the first row. As with low Reynolds number flow, the velocity profiles were further smoothed in the third row from enhanced mixing caused by the influence of upstream wakes.

### 3.2 Effect of streamwise spacing on time-dependent flowfield

One-dimensional energy spectra ( $E_{uu}$ ) were calculated to determine the frequency content in the cylinder wakes. The energy spectra were calculated using the streamwise velocity signal at a position in the pin-fin shear layers. For all high Reynolds number cases, the position chosen for calculating energy spectra was  $X/D = 0.9$ ,  $Y/D = 0.4$ . At low Reynolds number, especially in the first row wake, the shear layer was elongated relative to that of high Reynolds numbers. The point in the shear layer for calculating energy spectra was, therefore,  $X/D = 2$ ,  $Y/D = 0.4$  for low Reynolds number cases having  $S_L/D \geq 2.60$ . For  $S_L/D = 2.16$ , the interrogation position was  $X/D = 1.2$ ,  $Y/D = 0.4$ , and for  $S_L/D = 1.73$ , the interrogation point

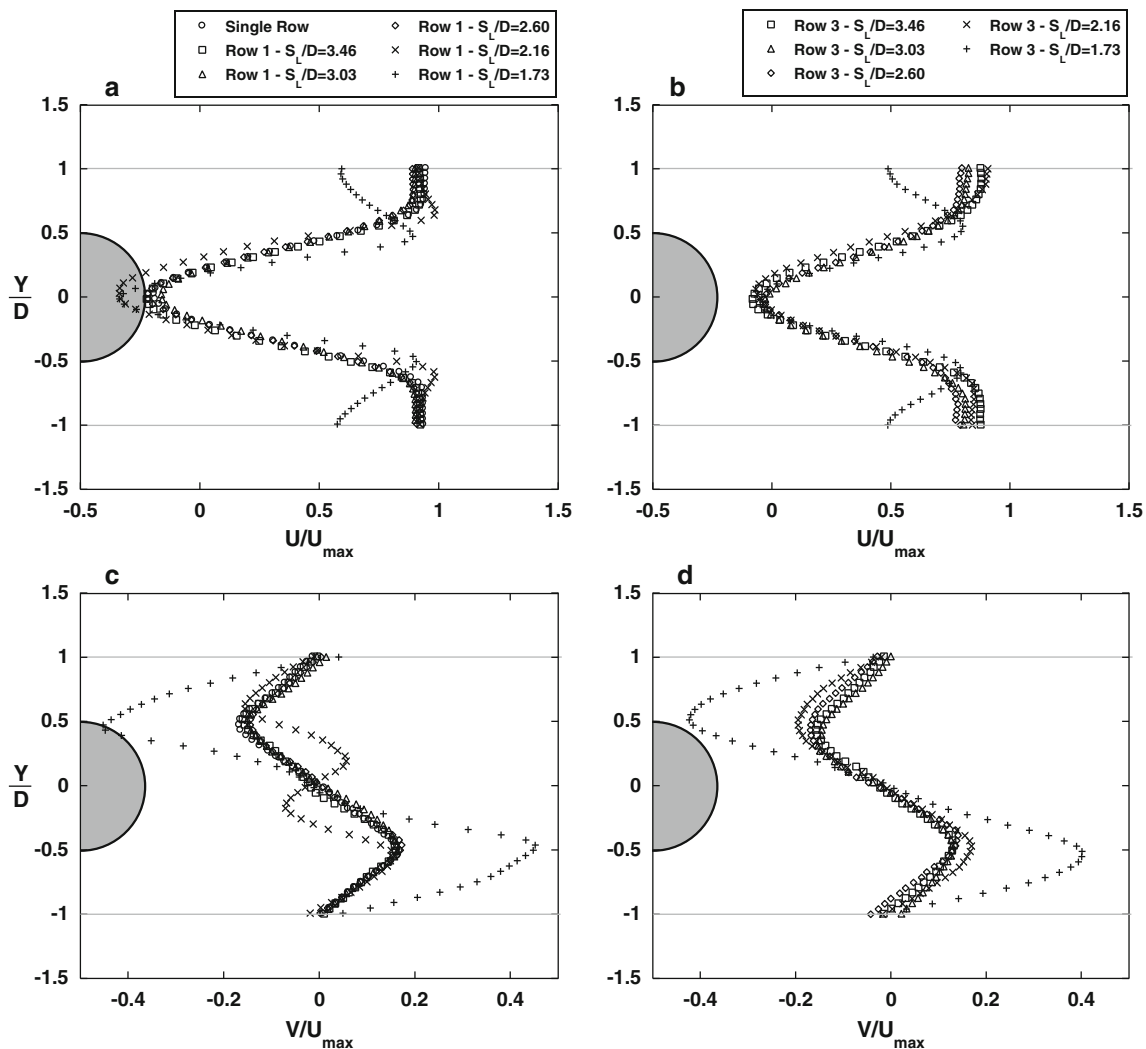


**Fig. 9** Mean velocity extracted at  $X/D = 1.0$  and  $Z/H = 0$  (channel symmetry plane) for  $Re_D = 2.0e4$ . Mean streamwise velocity for first and third row wakes is shown in (a) and (b), respectively. Mean

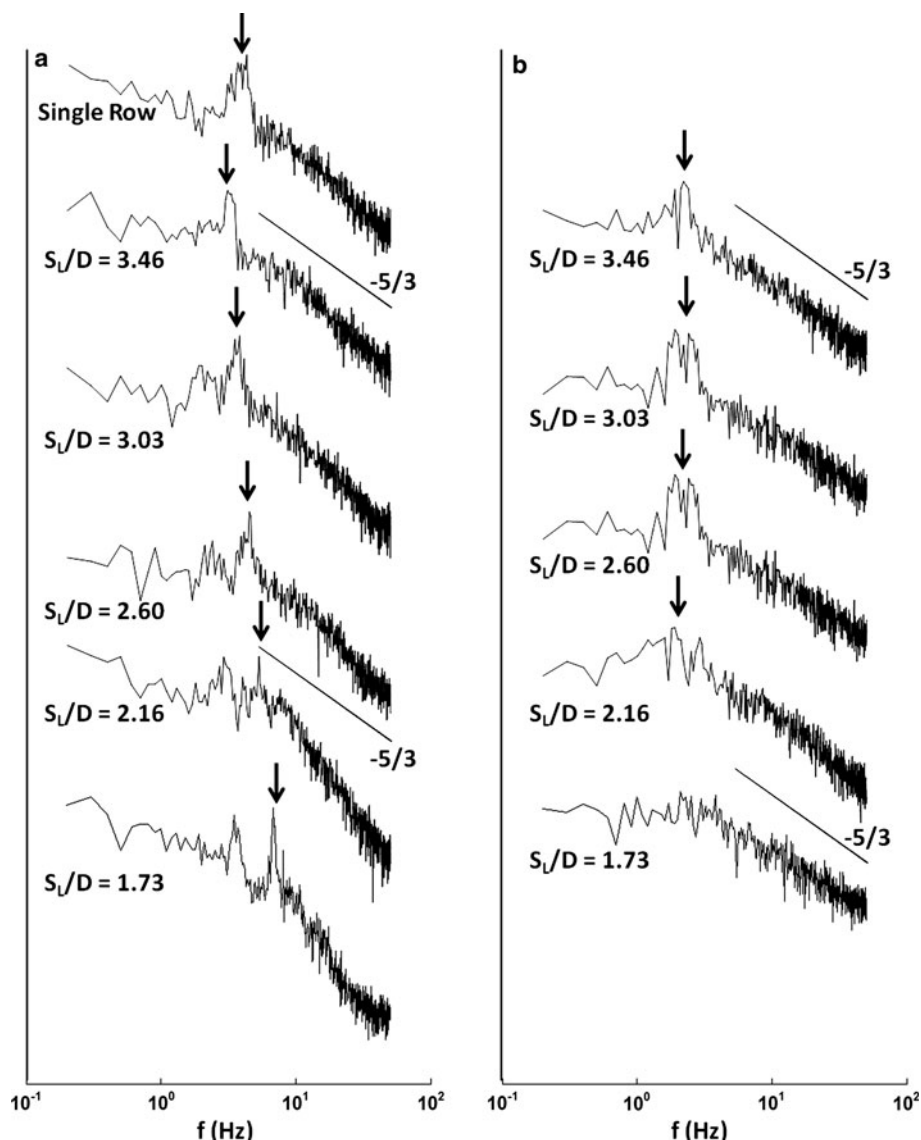
transverse velocity for first and third row wakes is shown in (c) and (d), respectively. Legends are common between (a) and (c) and between (b) and (d)

was  $X/D = 0.9$ ,  $Y/D = 0.4$ . A fast Fourier transform (FFT) was applied to the streamwise velocity signal. It was found that the use of a Hanning window resulted in a significant contribution of energy at low frequency that was on the same order as the lowest frequency scales in the flow. Although the identified shedding frequency was equivalent when comparing a rectangular window (no weighting) and a Hanning window, the rectangular window was used to eliminate the energy content at low frequency. One challenge of measuring energy spectra using TRDPV measurements was the short sample time, limited by memory when collecting high-resolution images at high frequency. Because of the short sample time, the energy spectra contained a substantial amount of noise. To reduce noise, the time signal of 3,000 data points was split into three signals, each having 1,000 points. The energy spectra from each of the 1,000-point time signals were then averaged. It

should be noted that the measured shedding frequency was equivalent when using a single time series having 1,000 or 3,000 samples. At the expense of reducing the frequency resolution, noise was reduced in the energy spectra when three 1,000-point signals were averaged together. Similarly, assuming symmetry about the wake axis, energy spectra were calculated at opposite sides of the wake. For example, data were collected at  $X/D = 0.9$ ,  $Y/D = 0.4$  in addition to  $X/D = 0.9$ ,  $Y/D = -0.4$ . The resulting energy spectra were then averaged using a total of six time signals, three time signals on each half of the wake.

The resulting spectra are shown in Figs. 10 and 11 for low and high Reynolds numbers, respectively. In Fig. 10, the one-dimensional energy spectra are shown for low Reynolds number where the first row wakes are shown in Fig. 10a and the third row wakes are shown in Fig. 10b. The shedding frequency in the first row was observed to

**Fig. 10** One-dimensional energy spectra ( $E_{uu}$ ) taken in the shear layer at  $Re_D = 3.0e3$  for **a** first row wakes and **b** third row wakes. Coordinate system is log–log and the shedding frequency is indicated with arrows

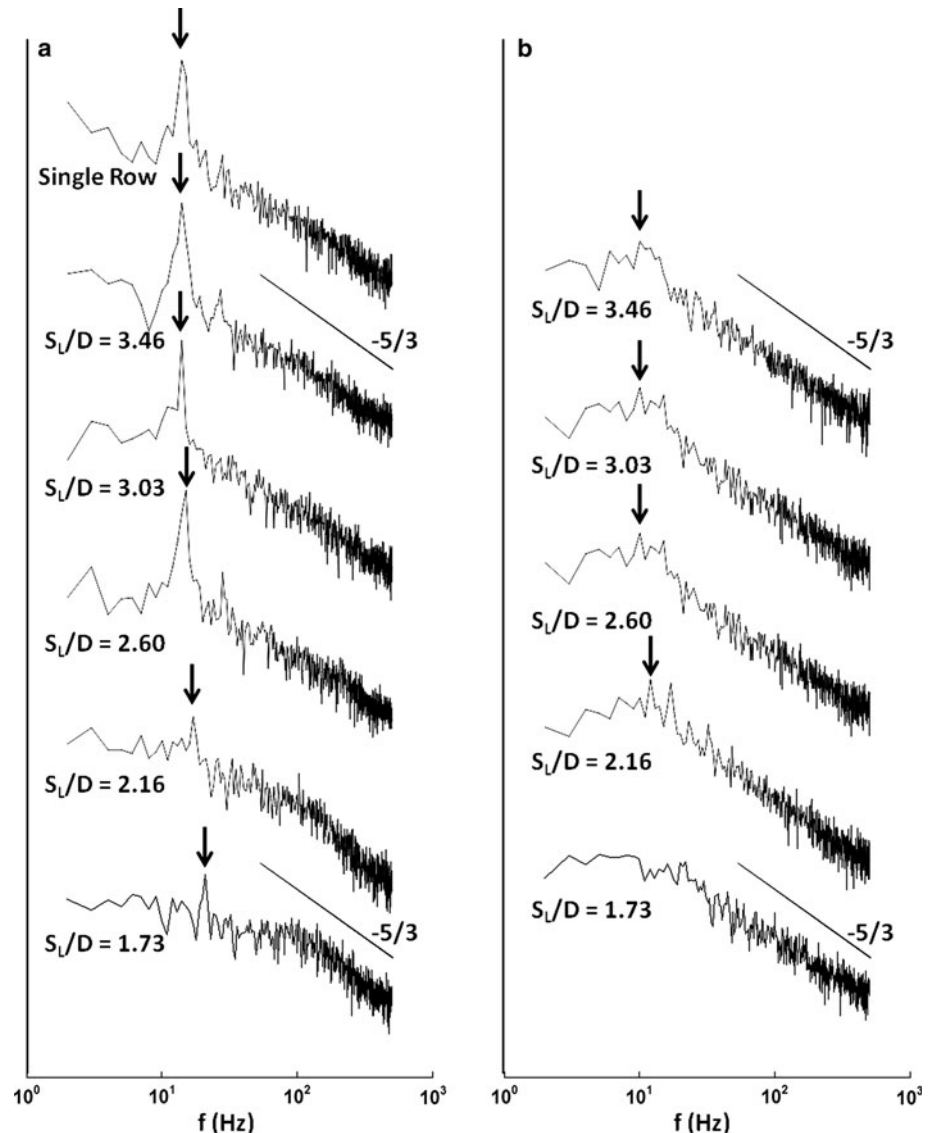


increase for decreasing  $S_L/D$ , as indicated by the arrows in Fig. 10. In the third row wakes, shown in Fig. 10b, the observed peaks in the energy spectra at the shedding frequency were broadened from interactions with the first row wake. Additionally, the peaks in the energy spectra of the third row were less sensitive to streamwise spacing than the first row. At high Reynolds number, the first row wakes in Fig. 11a showed that the shedding frequency increased for decreasing  $S_L/D$ . The peak in the energy spectra observed at the shedding frequency increased in magnitude for more widely spaced arrays. Similar to low Reynolds numbers, the spectral peak was broadened in the third row wakes at high Reynolds number, shown in Fig. 11b, from the wakes of upstream pin–fins.

The measured Strouhal frequency,  $St = fDU_{\max}^{-1}$ , increased for decreasing streamwise spacing, consistent with the work of Oengoren and Ziada (1998) who measured the

shedding frequency in long tube bundles. Constraining the wake effectively reduced the characteristic length scale and, subsequently, increased the characteristic frequency. Figure 12 shows the measured Strouhal frequency in the first row wake as a function of both Reynolds number and streamwise spacing. Despite the strong three-dimensional flow present in the short cylinder bundles, the shedding frequency measured at the channel midspan was in agreement with long tube bundles (Oengoren and Ziada 1998). The effect of Reynolds number was considered in the work of Oengoren and Ziada (1998) as shown by the two curves in Fig. 12. It should be noted that the single pin–fin row at low Reynolds number had  $St = 0.37$ , which was higher than the expected value of  $St = 0.21$  for a single, infinite cylinder (Norberg 2003). From Fig. 6, it was found that the single row had a shorter and narrower wake than the first row of cylinders having  $S_L/D = 3.46$ , which is consistent

**Fig. 11** One-dimensional energy spectra ( $E_{uu}$ ) taken in the shear layer  $Re_D = 2.0e4$  for **a** first row wakes and **b** third row wakes. Coordinate system is log–log and the shedding frequency is indicated with arrows



with the difference in Strouhal number. Simply stated, the presence of the second row of cylinders (for the case having  $S_L/D = 3.46$ ) elongated and widened the wake and, subsequently, caused a reduction in the shedding frequency, relative to the single row of cylinders. In contrast, increasing the streamwise spacing for high Reynolds number flows caused the Strouhal number to decrease monotonically and approach a constant value of  $St = 0.18$ .

Instantaneous streamlines and normalized vorticity contours are shown in Fig. 13 for the single pin–fin row. Figure 13a shows the instantaneous flow for low Reynolds number and Fig. 13b shows the instantaneous flow high Reynolds number. For the two cases in Fig. 13, snapshots were taken every one-fourth of a vortex shedding cycle, corresponding to the shedding frequency observed in the spectral analysis. Shear layer eddies and Kármán vortices

were labeled in Fig. 13 to illustrate the scale of these turbulent features. From visual inspection, the shear layer eddies had a length scale of approximately  $0.1D$  and Kármán vortices had a length scale approximately  $1D$ . Figure 13 shows the difference in the near wake flow when comparing  $Re_D = 3.0e3$  and  $2.0e4$ . At high Reynolds number, the Kármán vortices were clearly defined and occurred with periodicity. At low Reynolds number, however, the Kármán vortices were less well defined and the shedding motion was less periodic. Inspection of the instantaneous flowfield confirmed the assertion that near wake length correlated with shear layer stability. At low Reynolds number, Fig. 13a shows that the shear layer remains stable up to about  $X/D = 1$  before breaking down to turbulence. At high Reynolds number, however, Fig. 13b shows the shear layer transitioning to turbulence much closer to the point of separation, just prior to entering the

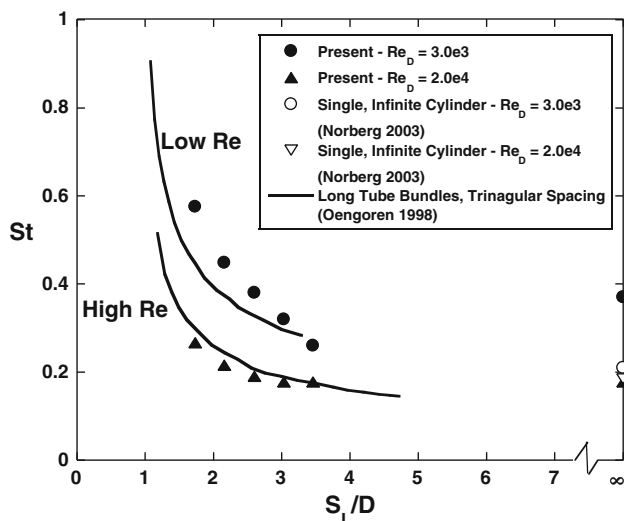


**Fig. 12** Strouhal number in the first row wake as a function of streamwise spacing and Reynolds number

TRDPIV domain. The stability of the shear layer at  $Re_D = 3.0e3$  resulted in a longer wake than that of  $Re_D = 2.0e4$ . It was also observed in the instantaneous flowfield snapshots that the turbulent scale was smaller at  $Re_D = 2.0e4$  than for  $Re_D = 3.0e3$ , as expected from turbulent scale considerations.

Figure 14 shows the instantaneous streamlines and normalized vorticity contours in the first row wake at  $S_L/D = 1.73$  for both  $Re_D = 3.0e3$  and  $2.0e4$ . The increment between snapshots, again, corresponded to one-fourth of the shedding frequency observed in the spectral analysis. Similar to the single row configurations in Figs. 13, 14 showed the formation of large structures resembling Kármán vortices. The structures that formed in first row wake of  $S_L/D = 1.73$ , however, did not shed with repeatability as with the single row case. Instead, the large structures observed in Fig. 14 surged forward and back along the shear layer. The two counter-rotating vortices switched leading and trailing positions with a quasi-periodic interval. Regardless of Reynolds number, the instantaneous near wake flow showed that there was a significant difference in the spatio-temporal evolution of the near wake for a single row of pin-fins and for pin-fins having  $S_L/D = 1.73$ .

Inspection of third row wakes at  $S_L/D = 1.73$ , shown in Fig. 15, revealed that the near wake was more turbulent than the first row wakes. The increment between snapshots in Fig. 15 was equal to that of Fig. 14. In the first row wakes, shown in Fig. 14, the differences between low and high Reynolds number flow were easily distinguishable. The Kármán vortices were more well defined at high Reynolds number while the shear layer was more stable for low Reynolds number. In the third row, however, Fig. 15 shows

less discernible differences between low and high Reynolds numbers. The amount of small-scale motion, for example, was similar for both low and high Reynolds numbers as shown in the contours of normalized vorticity. The Kármán vortices were well defined for both  $Re_D = 3.0e3$  and  $2.0e4$ . Additionally, vortex shedding in the third row wakes was quasi-periodic. The unsteady wakes from upstream pin-fins disrupted the formation of Kármán vortices in the third row wakes leading to a quasi-periodic vortex shedding pattern.

### 3.3 Effect of streamwise spacing on turbulence statistics

To investigate the distribution of turbulence in the pin-fin wakes, turbulent kinetic energy,  $k$ , was calculated using the in-plane, RMS velocity components as shown in Eq. 1.

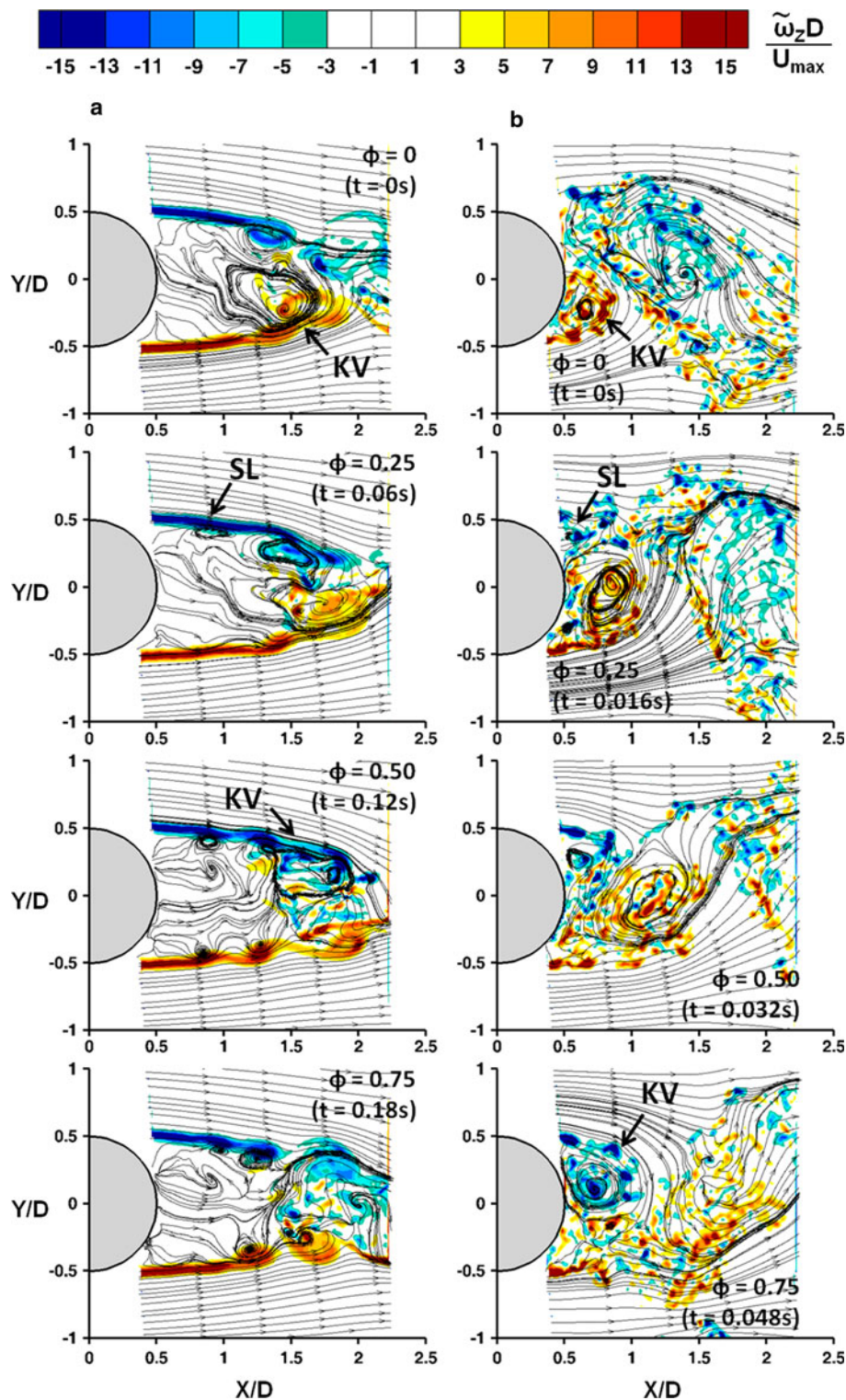
$$k = (u'^2 + v'^2)/2 \quad (1)$$

It should be noted that the RMS velocities in Eq. 1 are calculated from the ensemble-averaged velocities. Contours of normalized, turbulent kinetic energy are shown in Figs. 16 and 17 for  $Re_D = 3.0e3$  and  $2.0e4$ , respectively. For all cases, a band of increased turbulence was observed emerging tangent to the pin-fins as a result of Kelvin-Helmholtz instabilities along the shear layers. Regions of increased turbulence were also observed downstream of the pin-fins, along the wake axis where Kármán vortices formed.

In Fig. 16, at  $Re_D = 3.0e3$ , decreasing the streamwise spacing resulted in decreased  $k/U_{\max}^2$  magnitude in the first row wake. Contours of  $k/U_{\max}^2$  showed that the wake width narrowed for decreasing streamwise spacing. The single row case was an exception, because the single row wake showed a narrowed wake in comparison with the  $S_L/D = 3.46$  case. In the third row at  $Re_D = 3.0e3$ , the magnitude of  $k/U_{\max}^2$  increased relative to the first row. The disturbances from upstream wakes caused instability along the shear layers and allowed the Kármán vortices to form closer to the third row cylinder. The Kármán vortices in the third row wakes contributed to the increased  $k/U_{\max}^2$  in comparison with the shear-layer-driven first row wakes. The magnitude of  $k/U_{\max}^2$  in the third row decreased with decreasing  $S_L/D$ .

When  $Re_D$  was increased to  $2.0e4$ , the  $k/U_{\max}^2$  contours in Fig. 17 indicated that elevated turbulence occurred closer to the pin-fins in comparison with  $Re_D = 3.0e3$ , which was consistent with the wake length discussion. The  $k/U_{\max}^2$  levels in the first row wakes showed no significant dependence on streamwise spacing for  $S_L/D \geq 2.60$ . When  $S_L/D$  was reduced to 2.16, however, the  $k/U_{\max}^2$  levels in the wake were significantly attenuated in comparison with

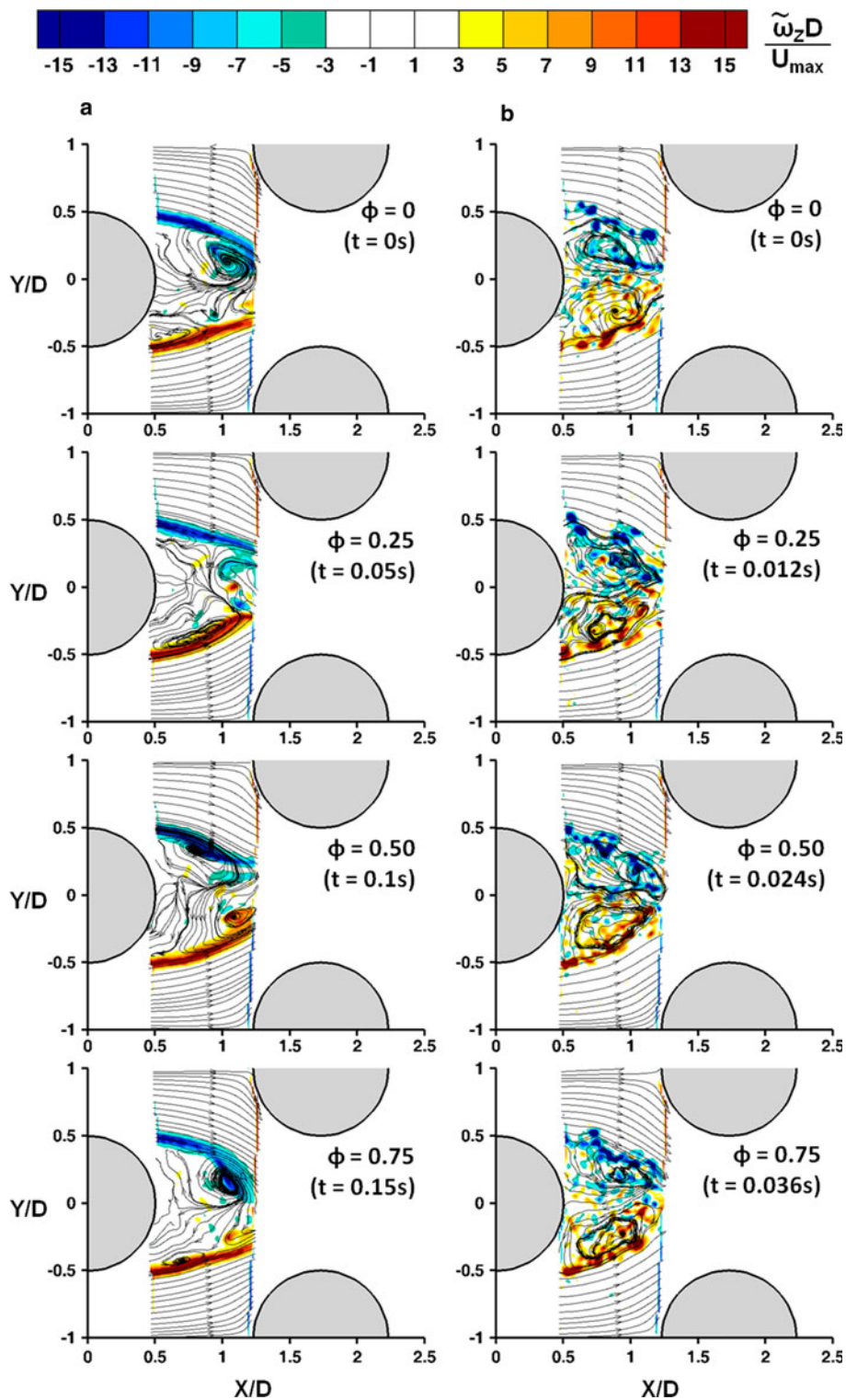
**Fig. 13** Instantaneous snapshots of wake shedding for single row of pin-fins at **a**  $Re_D = 3.0e3$  and **b**  $Re_D = 2.0e4$ . Snapshot increments are one-fourth of the vortex shedding cycle. Shear layer eddies and Kármán vortices are labeled to exemplify size and position of these turbulent features



$S_L/D = 2.60$ . The attenuated  $k/U_{\max}^2$  contours were in agreement with the spectral analysis in Fig. 11 which showed a significantly reduced spectral peak at the shedding frequency for  $S_L/D = 2.16$  in comparison with  $S_L/D = 2.60$  (by two orders of magnitude). In the third row wakes, the magnitude of  $k/U_{\max}^2$  contours was less than

that of the first row wakes. In contrast with low Reynolds number flow, the disturbances from upstream wakes disrupted the formation and shedding of Kármán vortices. Simply stated, the Kármán vortices were dominant in the first row (for  $S_L/D \geq 2.60$ ) and were broken up by upstream wakes in the third row.

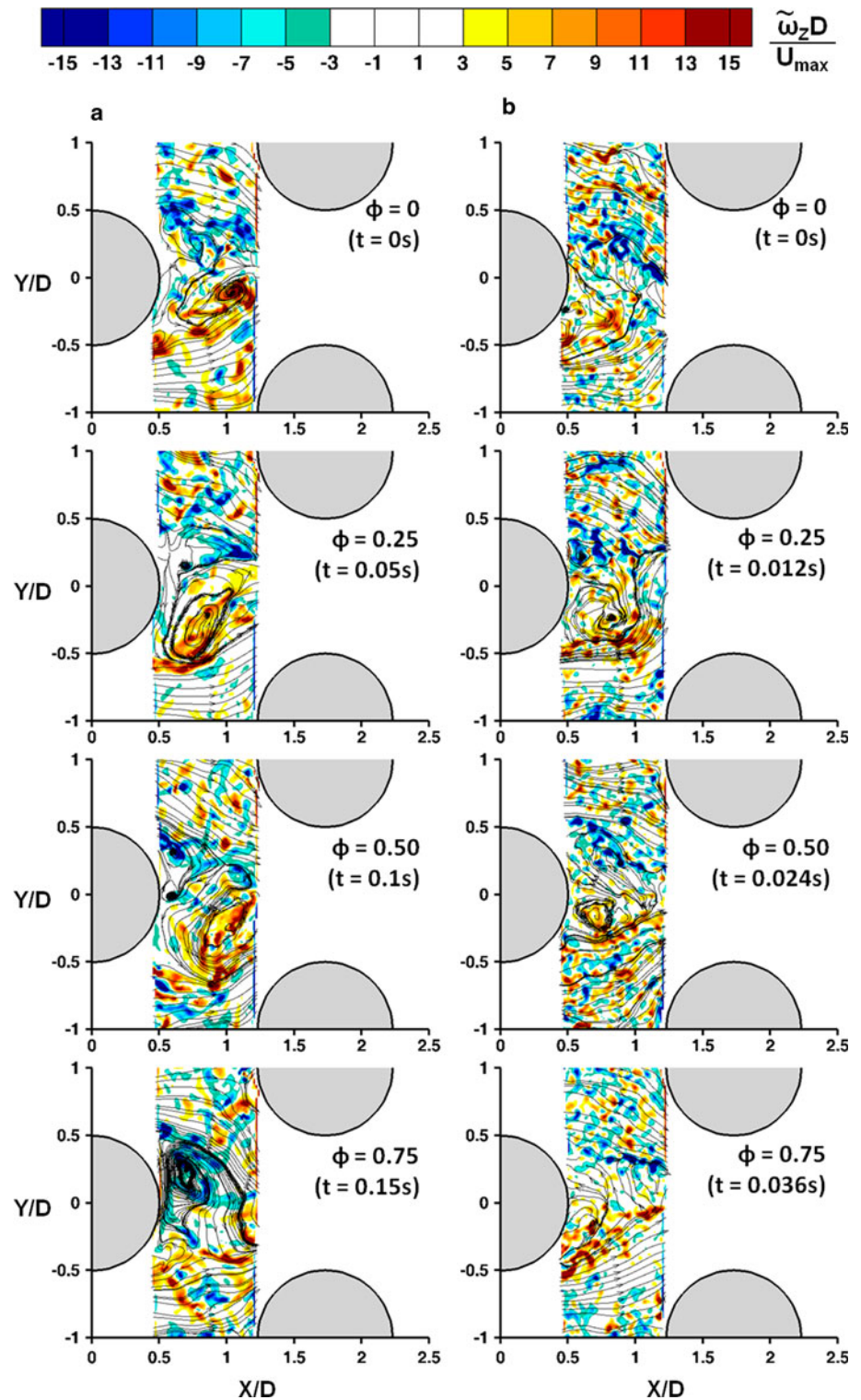
**Fig. 14** Instantaneous snapshots of wake shedding for the first row of pin-fins having  $S_t/D = 1.73$  at **a**  $Re_D = 3.0e3$  and **b**  $Re_D = 2.0e4$ . Snapshot increments are one-fourth of the vortex shedding cycle. Shear layer eddies and Kármán vortices are labeled to exemplify size and position of these turbulent features



The measured components of the Reynolds stress tensor in the near wake were computed to provide more detailed information on the momentum transport in the near wake. Fig. 18 and 19 show contours of the normal Reynolds stress component in the streamwise direction,  $\overline{u'u'}/U_{max}^2$ ,

for  $Re_D = 3.0e3$  and  $2.0e4$ , respectively. Both shear layer eddies (SL) and Kármán vortices (KV) contributed  $\overline{u'u'}/U_{max}^2$ , as indicated in Fig. 18. Along the shear layers,  $\overline{u'u'}/U_{max}^2$  was elevated from the formation of shear layer eddies. Beyond the position  $X/D = 1.5$ , the Kármán

**Fig. 15** Instantaneous snapshots of wake shedding for the third row of pin-fins having  $S_L/D = 1.73$  at **a**  $Re_D = 3.0e3$  and **b**  $Re_D = 2.0e4$ . Snapshot increments are one-fourth of the vortex shedding cycle



vortices began to form and contributed to increased  $\overline{u'u'}/U_{\max}^2$ . As streamwise spacing was reduced, the shear layers became more stable in the first row, indicated by the reduced magnitude of  $\overline{u'u'}/U_{\max}^2$  along the shear layers. In the third row, the shear layers were less stable than those of the first row, as expected from the disturbances generated

upstream. Consistent with previous discussions, Fig. 19 shows that the first row wake at high Reynolds number was shortened and more unsteady shear layer when compared with low Reynolds number flow. The strong presence of vortex shedding in the first row at high Reynolds number resulted in a V-shaped pattern of  $\overline{u'u'}/U_{\max}^2$ , as indicated in

**Fig. 16** Contours of normalized, in-plane turbulent kinetic energy at  $Re_D = 3.0e3$

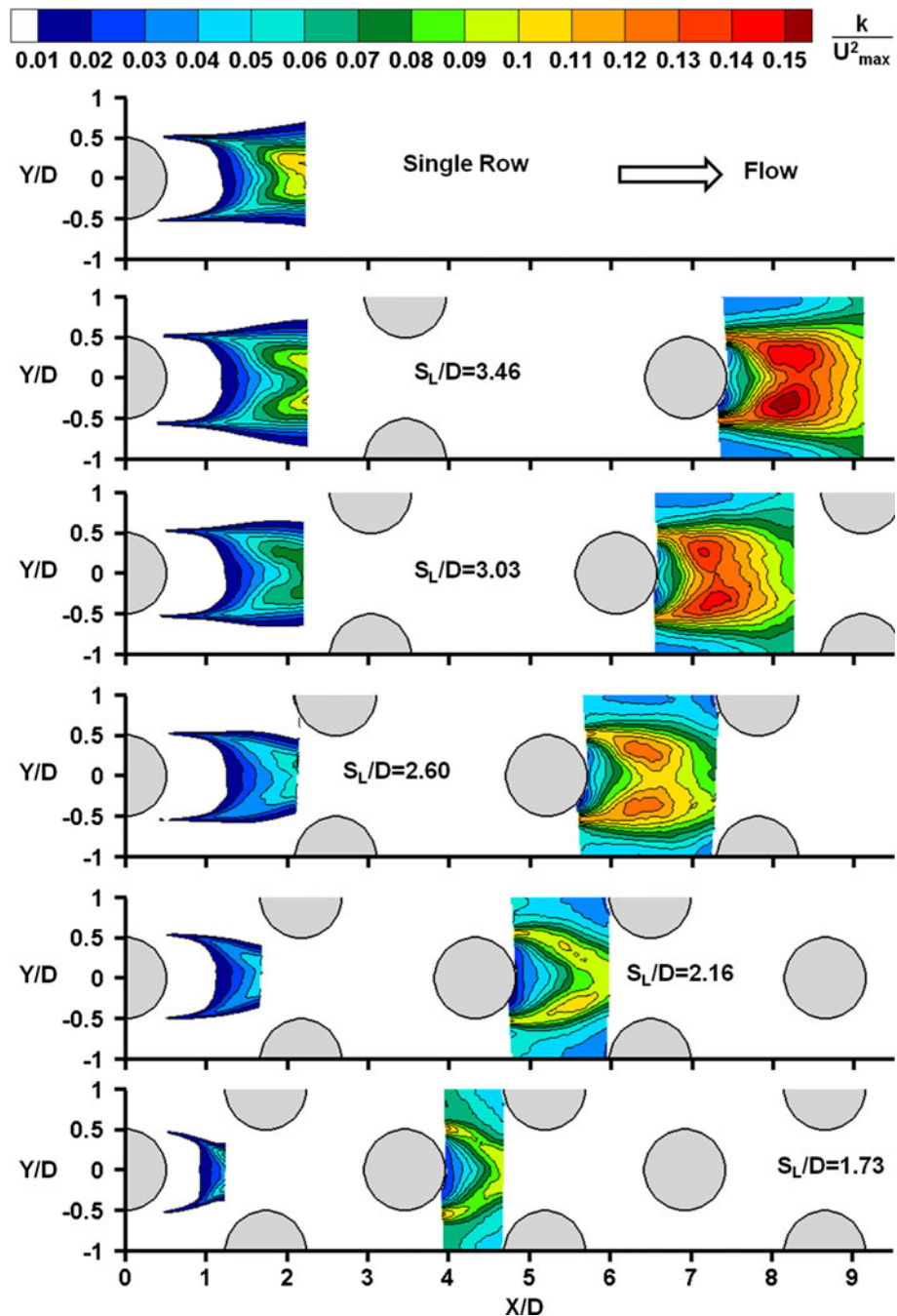
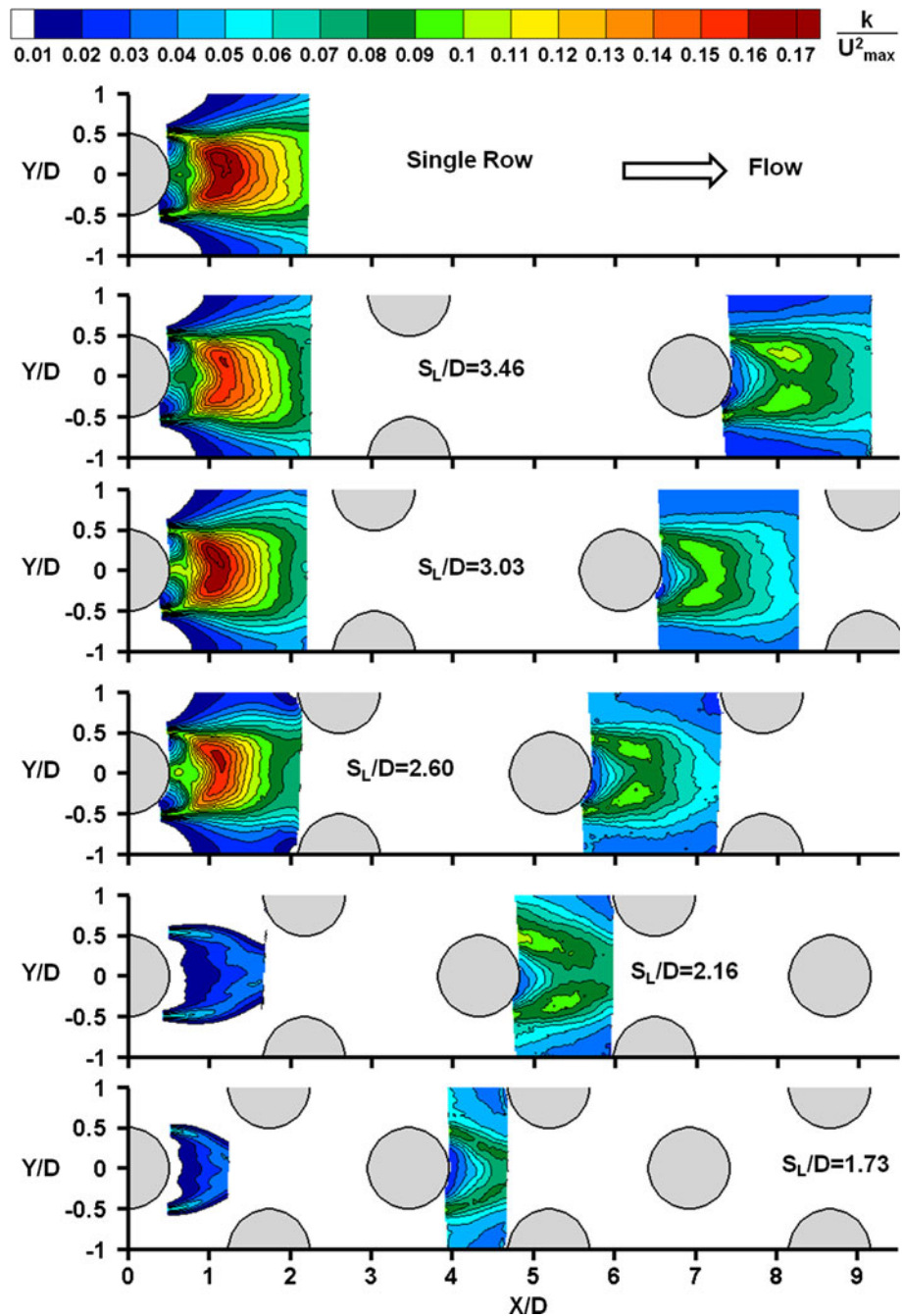


Fig. 19. Although the magnitude of  $\overline{u'u'}/U_{\max}^2$  was similar for cases having  $S_L/D \geq 2.60$ , the second row pin-fins were observed to dampen  $\overline{u'u'}/U_{\max}^2$  fluctuations for  $S_L/D = 2.60$  and, to a lesser extent,  $S_L/D = 3.03$ . The attenuation of vortex shedding was observed in the first row when  $S_L/D$  was reduced to 2.16, consistent with contours of turbulent kinetic energy. The third row wakes at high Reynolds number showed similar contours of  $\overline{u'u'}/U_{\max}^2$  as  $S_L/D$  was reduced, although the magnitude of  $\overline{u'u'}/U_{\max}^2$  decreased with decreasing  $S_L/D$ .

Figures 20 and 21 show contours of the normal Reynolds stress component in the transverse direction,  $\overline{v'v'}/U_{\max}^2$ , for  $Re_D = 3.0e3$  and  $2.0e4$ , respectively. The vortex shedding motion contributed to elevated  $\overline{v'v'}/U_{\max}^2$  along the wake axis, as indicated in Figs. 20 and 21. At low Reynolds number, Fig. 20 shows that decreasing streamwise spacing reduced the magnitude of  $\overline{v'v'}/U_{\max}^2$  in the wake. One exception was observed in the third row wake for the streamwise spacing,  $S_L/D = 2.16$ . At high Reynolds number, contours of  $\overline{v'v'}/U_{\max}^2$  were

**Fig. 17** Contours of normalized, in-plane turbulent kinetic energy at  $Re_D = 2.0e4$

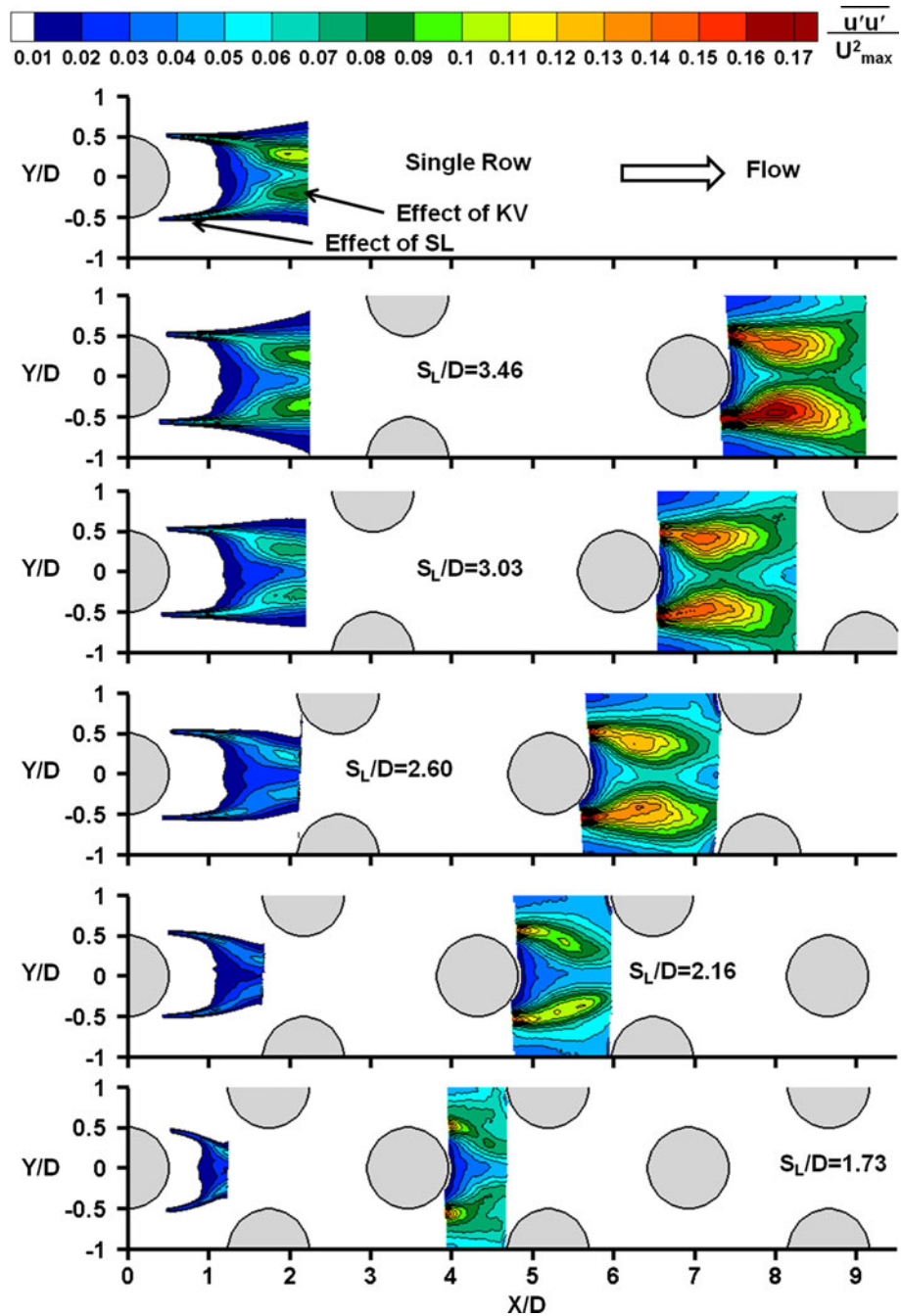


dominated by the vortex shedding motion. For cases where vortex shedding was attenuated ( $S_L/D \leq 2.16$ ), however, Fig. 21 shows that the shear layer eddies were the primary source of  $\overline{v'v'}/U_{\max}^2$ . Consistent with previous discussions, the level of  $\overline{v'v'}/U_{\max}^2$  decreased with decreasing streamwise spacing in the third row wakes at high Reynolds number.

Figures 22 and 23 show contours of Reynolds shear stress,  $\overline{u'v'}/U_{\max}^2$ , for  $Re_D = 3.0e3$  and  $2.0e4$ , respectively. Although the shear layer eddies contributed to Reynolds shear stress (high Reynolds number, close spacings),

Figs. 22 and 23 show that the magnitude of Reynolds shear stress correlated with the strength of vortex shedding. For example, Reynolds stress increased in the third row relative to the first row for low Reynolds number flow. As mentioned previously, disturbances from upstream rows caused instability in the shear layers which was beneficial for the Kármán vortices in the third row. It should be noted, for  $S_L/D = 1.73$ , that a region of elevated Reynolds shear stress was observed in the third row wake which was caused by the Reynolds shear stress produced in the second row. Figure 23 illustrates the Reynolds shear stress from

**Fig. 18** Contours of normalized  $\overline{u'u'}$  Reynolds stress at  $Re_D = 3.0e3$

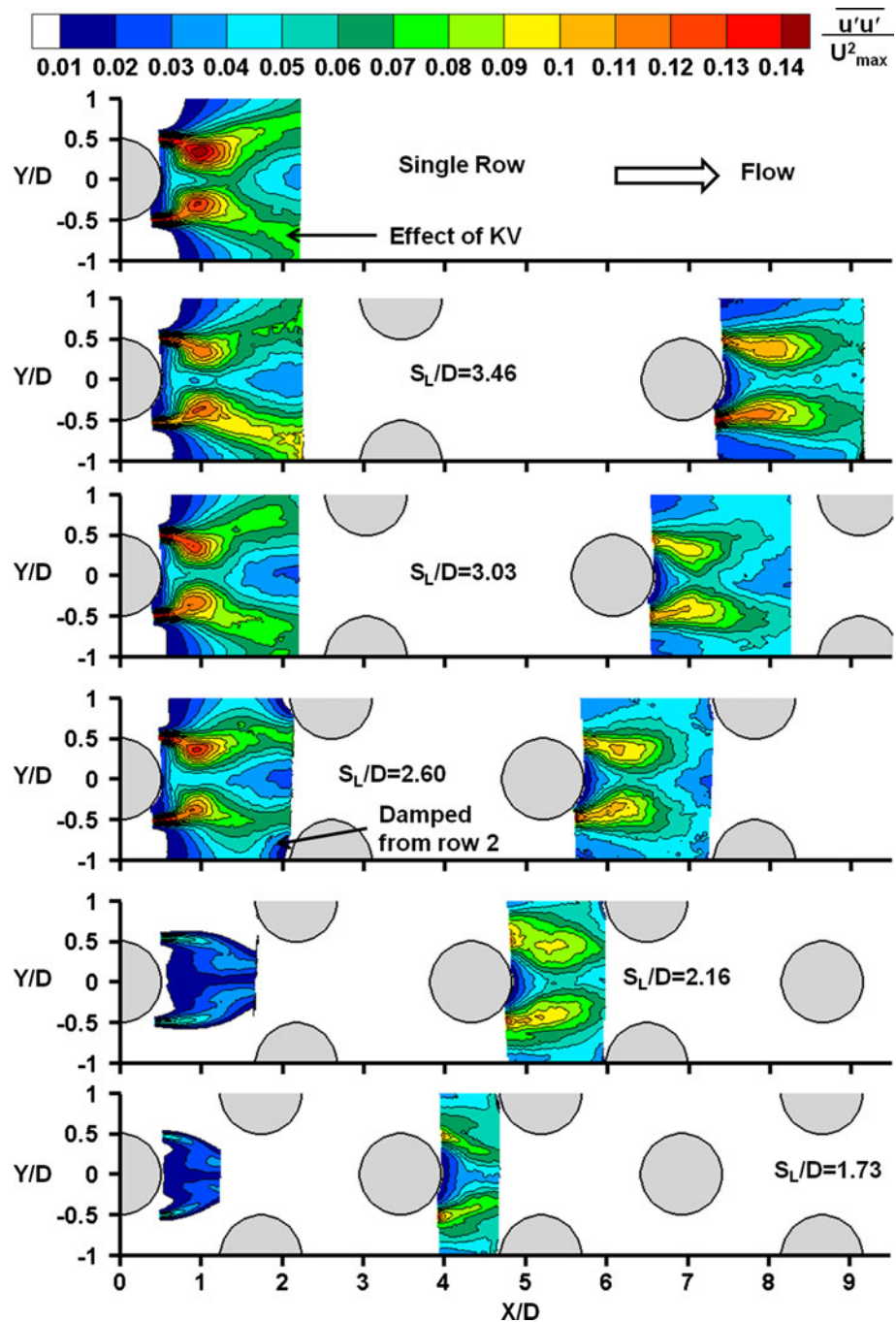


the second row observed in the third row wake. This phenomenon was noticeable for  $S_L/D = 1.73$  and 2.16. Reynolds stress decreased in the third row relative to the first row at high Reynolds number. Vortex shedding was the dominant motion in the first row wake and contributed to elevated  $\overline{u'v'}/U_{\max}^2$ . In the third row wakes, however, the disturbances from upstream rows broke up vortex shedding and caused quasi-periodic shedding. Consistent with previous discussions, the level of Reynolds shear stress decreased with decreasing streamwise spacing at

low Reynolds number. At high Reynolds number, the first row wakes were independent of streamwise spacing until  $S_L/D$  was reduced to 2.16, where shedding was attenuated. In the third row wakes, the magnitude of Reynolds shear stress decreased with decreasing streamwise spacing.

Previous studies have shown that heat transfer in pin–fin heat exchangers increases with decreasing streamwise spacing (Metzger et al. 1986; Lawson et al. 2011; Ostanek and Thole 2012). In the present work, the flowfield was

**Fig. 19** Contours of normalized  $\overline{u'u'}$  Reynolds stress at  $Re_D = 2.0e4$

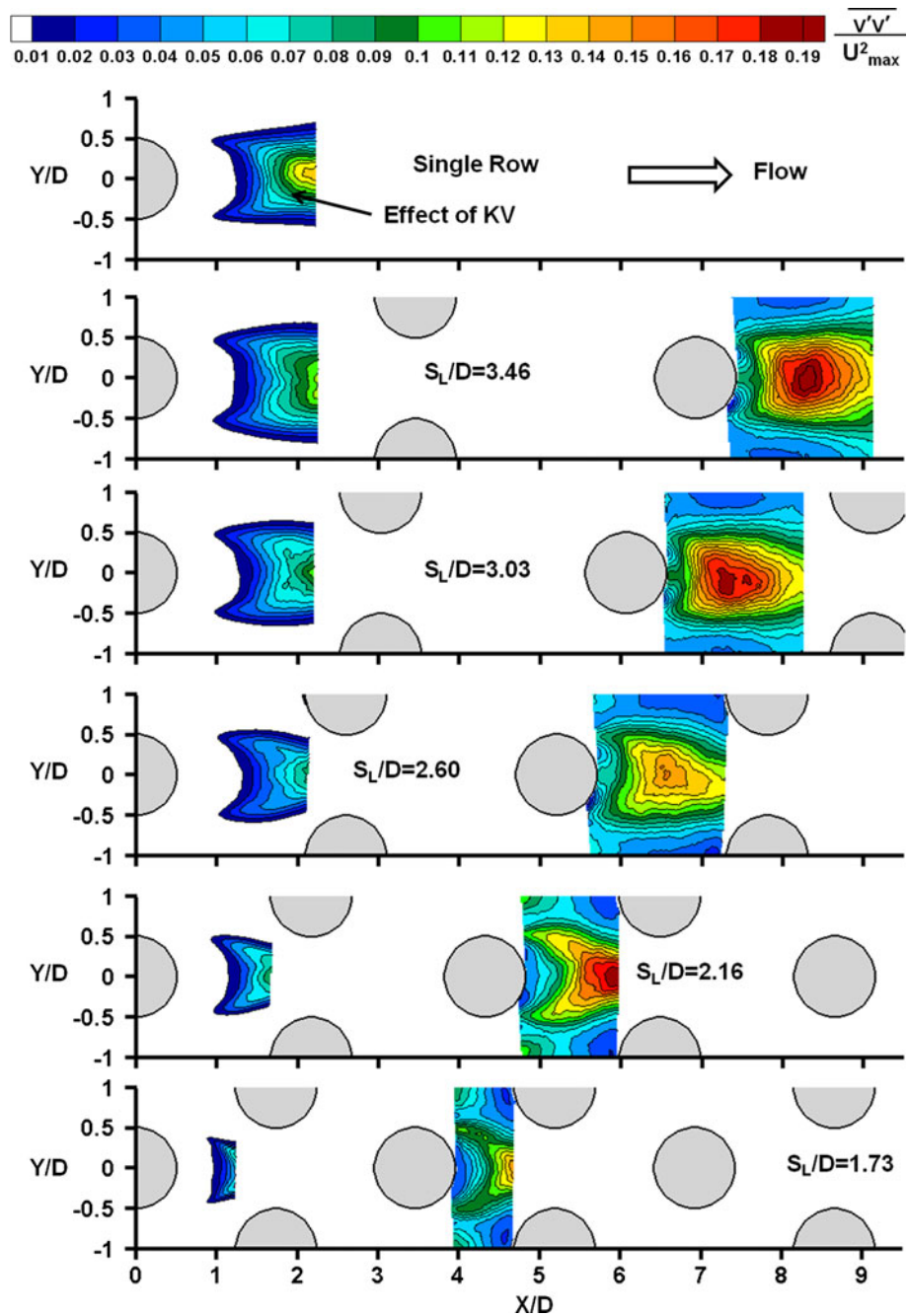


investigated for typical pin–fin geometries where the streamwise spacing was varied. The most important flow-field feature observed in the present work was the attenuation of vortex shedding in the first row at high Reynolds number when streamwise spacing was reduced to  $S_L/D = 2.16$ . Heat transfer in the first row, however, has been shown to be less dependent on streamwise spacing than the rows in the developed portion of the array (Lawson et al. 2011; Ostanek and Thole 2012). Simply stated, the major

flowfield regime change observed in the present work has little influence on heat transfer in the first row of a pin–fin array.

When considering the present flowfield measurements made in the developed portion of the array (third row and beyond), the third row wakes showed no major flow regime changes. The effect of streamwise spacing on the third row wakes was mainly observed in the reduction of turbulent kinetic energy. Although decreasing streamwise

**Fig. 20** Contours of normalized  $\overline{v'v'}$  Reynolds stress at  $Re_D = 3.0e3$

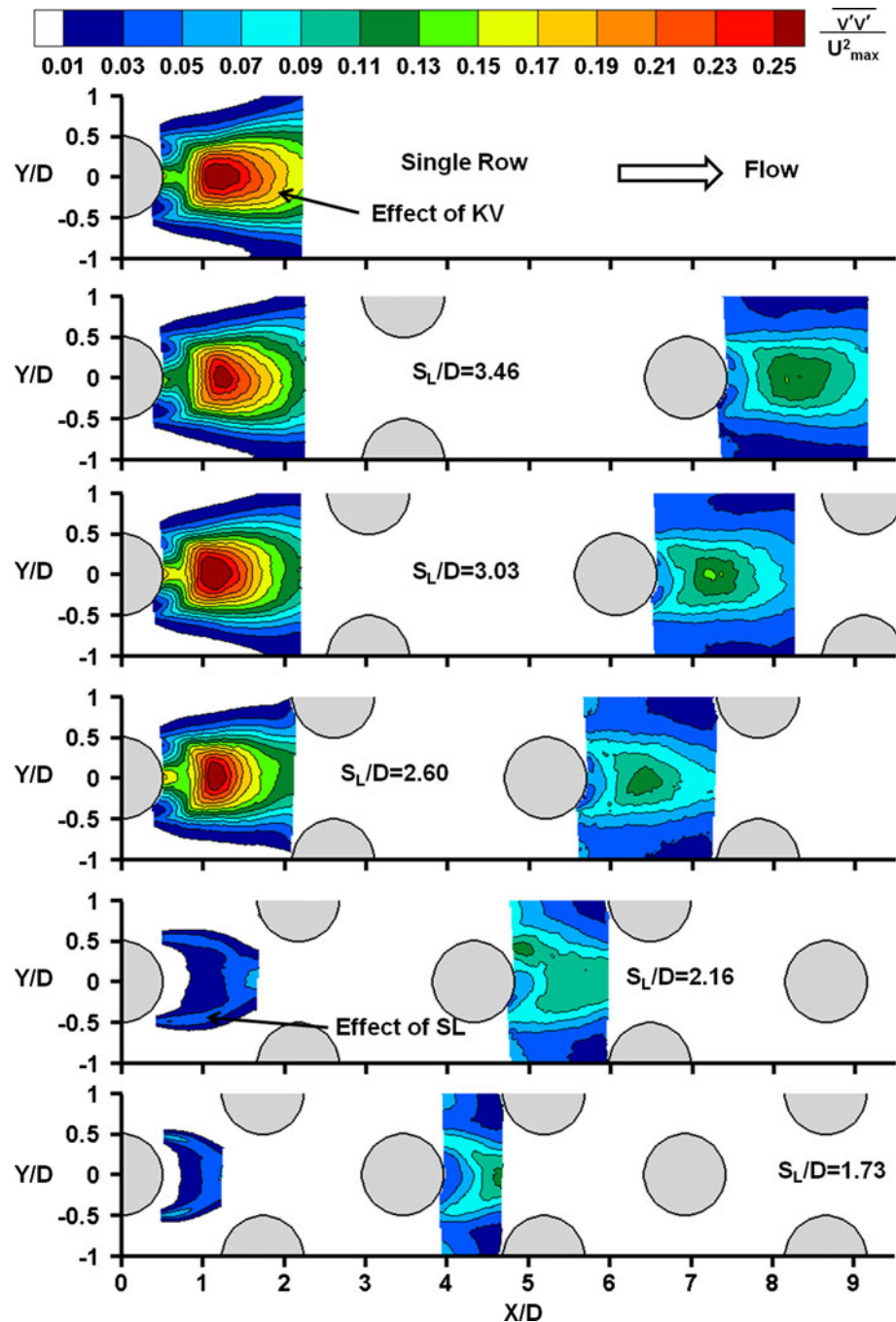


spacing increases heat transfer, the level of turbulent kinetic energy *decreases*. It should be noted that the turbulent kinetic energy quantified in the present work includes both periodic unsteadiness (vortex shedding) and random unsteadiness (turbulence). Further investigation is required to determine the mechanism causing high heat transfer coefficients for closer streamwise spacing. Three-dimensional effects may be a significant factor as well as the relative contribution of periodic unsteadiness versus random unsteadiness.

#### 4 Conclusions

The near wake behavior was investigated for pin–fin arrays having transverse spacing of two diameters and height-to-diameter ratio of unity. Six geometric configurations were considered including a single row of pin–fins and five multiple-row arrays having streamwise spacings between 1.73 and 3.46 diameters. It was found that the wake closure position was reduced for a single row of pin–fins when compared with a single, infinite cylinder because

**Fig. 21** Contours of normalized  $\overline{v'v'}$  Reynolds stress at  $Re_D = 2.0e4$



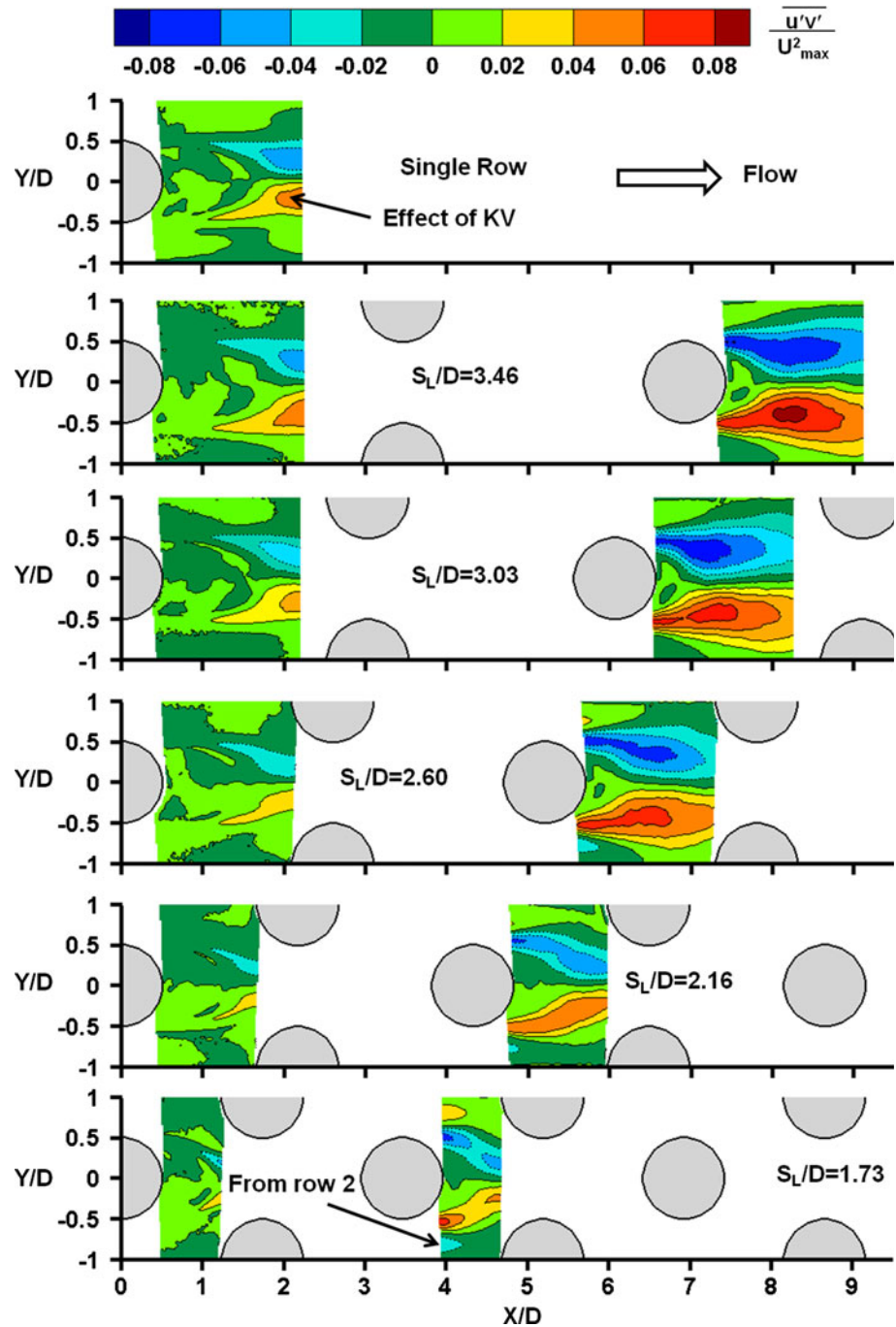
of turbulence generated at the channel walls. In the third pin–fin row, wake closure position was reduced relative to a single, infinite cylinder to a greater extent than the first row wakes because of turbulence generated by the unsteady wakes of upstream pin–fins.

The vortex shedding frequency was found to increase for decreasing streamwise spacing. As the near wake was constrained by decreasing streamwise spacing, the characteristic length scales in the near wake decreased and, subsequently, the characteristic frequency increased. The Strouhal frequency decreased when Reynolds number was

increased from  $3.0e3$  to  $2.0e4$ , and the influence of streamwise spacing on the Strouhal number was more apparent at low Reynolds numbers.

At low Reynolds number, turbulent kinetic energy increased in the third row relative to the first row. Disturbances generated in upstream rows caused instability in the shear layers which promoted the formation of Kármán vortices. At high Reynolds number, however, turbulent kinetic energy decreased in the third row relative to the first row. The first row was dominated by periodic vortex shedding and disturbances from upstream wakes broke up

**Fig. 22** Contours of normalized  $\overline{u'v'}$  Reynolds stress at  $Re_D = 3.0e3$



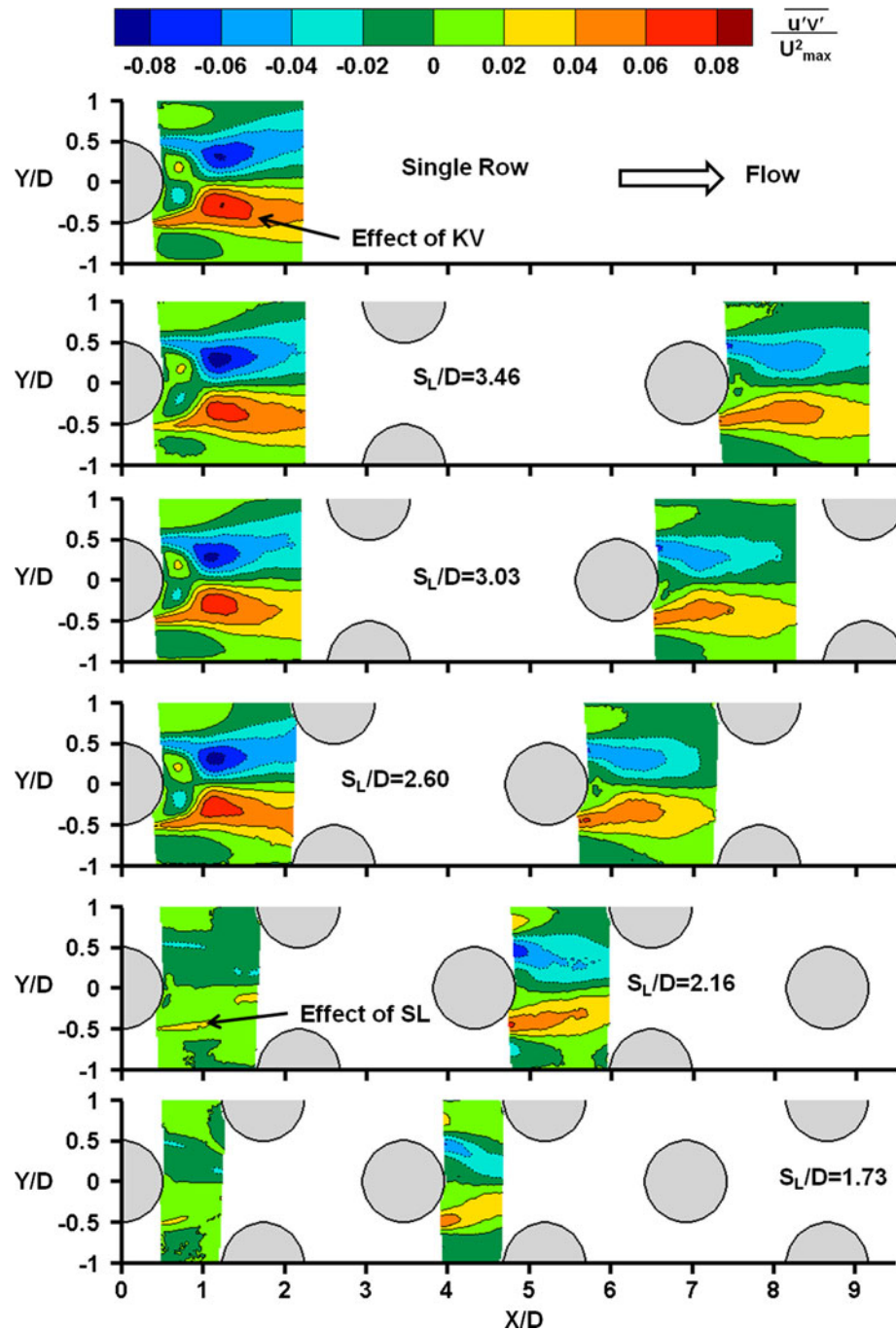
the formation of Kármán vortices in the third row, resulting in a quasi-periodic shedding motion.

A significant change in the near wake behavior was observed at high Reynolds number when streamwise spacing was reduced from  $S_L/D = 2.60$ – $2.16$ . At high Reynolds number, vortex shedding was the dominant motion in the wake for  $S_L/D \geq 2.60$ . When  $S_L/D$  was reduced to 2.16, however, vortex shedding was attenuated. The peak in the energy spectrum at the vortex shedding frequency was two orders of magnitude lower for

$S_L/D = 2.16$  compared to  $S_L/D \geq 2.60$ . Additionally, contours of turbulent kinetic energy and Reynolds shear stress were significantly reduced for  $S_L/D = 2.16$  compared to  $S_L/D \geq 2.60$ .

When comparing the present flowfield measurements to previous pin–fin heat transfer measurements, it was found that the near wake behavior in the first row had no significant influence on the heat transfer in the first row. At high Reynolds number, periodic shedding was present for  $S_L/D = 2.60$  while shedding was attenuated for  $S_L/D = 2.16$ .

**Fig. 23** Contours of normalized  $\overline{u'v'}$  Reynolds stress at  $Re_D = 2.0e4$



Despite the difference in flowfield behavior, first row heat transfer was shown to be relatively independent of streamwise spacing. The developed rows of pin–fin arrays are known to have increased heat transfer coefficients for reduced streamwise spacing. The present flowfield measurements, however, showed that the level of turbulent kinetic energy decreased for decreasing streamwise spacing. Further investigation is required to determine whether three-dimensional effects or the relative influence of periodic versus random unsteadiness contribute to heat transfer.

**Acknowledgments** The authors would like to acknowledge the Department of Defense and the SMART fellowship program for providing funding for this work.

## References

- Aiba S, Tsuchida H, Ota T (1982) Heat transfer around tubes in staggered tube banks. *Bull JSME* 25(204):927–933
- Ames FE, Dvorak LA (2006a) The influence of reynolds number and row position on surface pressure distributions in staggered pin fin

- arrays. Paper presented at the ASME Turbo Expo 2006, Barcelona, Spain
- Ames FE, Dvorak LA (2006b) Turbulent transport in pin fin arrays—experimental data and predictions. *J Turbomach* 128(1):71–81
- Ames FE, Nordquist CA, Klennert LA (2007) Endwall heat transfer measurements in a staggered pin fin array with an adiabatic pin. Paper presented at the ASME Turbo Expo 2007, Montreal, Canada
- Chyu MK, Siw SC, Moon HK (2009) Effects of height-to-diameter ratio of pin element on heat transfer from staggered pin–fin arrays. Paper presented at the ASME Turbo Expo 2009, Orlando, FL
- Delibra G, Hanjalic K, Borello D, Rispoli F (2010) Vortex structures and heat transfer in a wall-bounded pin matrix: LES with a RANS wall-treatment. *Int J Heat Fluid Flow* 31(5):740–753
- Iwaki C, Cheong KH, Monji H, Matsui G (2004) PIV measurement of the vertical cross-flow structure over tube bundles. *Exp Fluids* 37(Compendex):350–363
- Lawson SA, Thrift AA, Thole KA, Kohli A (2011) Heat transfer from multiple row arrays of low aspect ratio pin fins. *Int J Heat Mass Transf* 54(17–18):4099–4109
- Lyll ME, Thrift AA, Thole KA, Kohli A (2011) Heat transfer from low aspect ratio pin fins. *J Turbomach* 133(1):1–10
- Metzger DE, Haley SW (1982) Heat transfer experiments and flow visualization for arrays of short pin fins. Paper presented at the ASME Turbo Expo 1982, London, United Kingdom
- Metzger DE, Berry RA, Bronson JP (1982) Developing heat transfer in rectangular ducts with staggered arrays of short pin fins. *J Heat Transfer* 104(4):700–706
- Metzger DE, Shepard WB, Haley SW (1986) Row Resolved heat transfer variations in pin–fin arrays including effects of non-uniform arrays and flow convergence. Paper presented at the ASME Turbo Expo, 1986, Duesseldorf, W. Germany
- Moffat RJ (1988) Describing the uncertainties in experimental results. *Exp Thermal Fluid Sci* 1(1):3–17
- Nogueira J, Lecuona A, Rodriguez PA (1997) Data validation, false vectors correction and derived magnitudes calculation on PIV data. *Meas Sci Technol* 8(12):1493–1501
- Norberg C (1998) LDV-measurements in the near wake of a circular cylinder. In: *Advances in understanding of bluff body wakes and vortex-induced vibration*, Washington D.C
- Norberg C (2003) Fluctuating lift on a circular cylinder: review and new measurements. *J Fluids Struct* 17(1):57–96
- Oengoren A, Ziada S (1998) An in-depth study of vortex shedding, acoustic resonance and turbulent forces in normal triangle tube arrays. *J Fluids Struct* 12(Compendex):717–758
- Ostaneck JK, Thole KA (2011) Flowfield measurements in a single row of low aspect ratio pin–fins. Paper presented at the ASME Turbo Expo 2011, Vancouver, Canada. Paper accepted for publication in the *Journal of Turbomachinery*
- Ostaneck JK, Thole KA (2012) Effects of Varying streamwise and spanwise spacing in pin–fin arrays. Paper presented at the ASME Turbo Expo, 2012, Copenhagen, Denmark
- Ozturk NA, Akkoca A, Sahin B (2008) PIV measurements of flow past a confined cylinder. *Exp Fluids* 44(6):1001–1014
- Paul SS, Tachie MF, Ormiston SJ (2007) Experimental study of turbulent cross-flow in a staggered tube bundle using particle image velocimetry. *Int J Heat Fluid Flow* 28(3):441–453
- Polak DR, Weaver DS (1995) Vortex shedding in normal triangular tube arrays. *J Fluids Struct* 9(1):1
- Scarano F, Riethmuller ML (2000) Advances in iterative multigrid PIV image processing. *Exp Fluids* 29(Supplement 1):S051–S060
- Simoneau RJ, VanFossen GJ Jr (1984) Effect of location in an array on heat transfer to a short cylinder in crossflow. *J Heat Transfer* 106(1):42–48
- Szepessy S, Bearman PW (1992) Aspect ratio and end plate effects on vortex shedding from a circular cylinder. *J Fluid Mech* 234(1):191–217
- Weaver DS, Lian HY, Huang XY (1993) Vortex shedding in rotated square arrays. *J Fluids Struct* 7(2):107–121
- Zdravkovich MM (1997) *Flow around circular cylinders—volume 1: introduction*. Oxford University Press, New York, NY
- Zdravkovich MM, Namork JE (1979) Structure of interstitial flow between closely spaced tubes in staggered array. In: *Flow induced vibration, symposium presented at the national congress on pressure vessel and piping technology, 3rd, San Francisco, CA, USA, 1979*. ASME, pp 41–46